Analysis of $D^{*0} \to D^0(K^-\pi^+)\ \pi^0(\gamma\gamma)$ in Belle-II experiment

Thesis submitted in partial fulfillment for the award of degree of

Master of Science in **Physics**

by

Aritra Paul
Roll no.: 20PH05004

Under the supervision of
Dr. Seema Bahinipati

Department of Physics
SCHOOL OF BASIC SCIENCES
INDIAN INSTITUTE OF TECHNOLOGY BHUBANESWAR

May 13, 2022

Certificate

This is to certify that the work contained in this report entitled **"Analysis of** $D^{*0} \rightarrow D^0(K^-\pi^+)\,\pi^0(\gamma\gamma)$ **in Belle-II experiment"** submitted by **Aritra Paul** having roll number **20PH05004** to School of Basic Sciences, Indian Institute of Technology Bhubaneswar towards the requirement of the course **PHD002 Project** has been carried out by him under my supervision and I consider it worthy of consideration for the award of the degree of **Master of Science** in the Institute.

Dr. Seema Bahinipati
Assistant Professor
School of Basic Sciences
Indian Institute of Technology Bhubaneswar
May 13, 2022

Declaration

I certify that

- This work has not been submitted to any other institute for any other degree or diploma.
- I have followed the guidelines given in the Ethical code of conduct of the Institute.
- Whenever I have used materials from other sources, I have given due credit to them by citing them in the text of the project and giving their details in the references.
- Whenever I have quoted written materials from other sources, I have put them under quotation and given due credit to the source by citing them and by giving required details in the references.

Aritra Paul

Acknowledgement

I am grateful to my supervisor, Dr. Seema Bahinipati for allowing me to work on this project and for giving me the opportunity to be a part of a leading high energy collaboration like Belle-II. Without her continuous support, guidance and encouragement throughout the duration of this project, this work would not be possible. I would also like to thank my seniors Mr. Souvik Maity, Mr. Rishabh Raturi and Mr. Samarendra Nayak at the Experimental High Energy Physics (EHEP) laboratory in The School of Basic Sciences, IIT Bhubaneswar for their help and assistance. I would also like to take this opportunity to thank my colleague Arnab Das. Discussions with him helped me to gain clarity in many concepts and enabled me to execute my work more efficiently.

Finally, I would like to thank my parents for their love,support and constant motivation.

Abstract

The decay mode $D^{*0} \to D^0(K^-\pi^+)\pi^0(\gamma\gamma)$ has been studied using $100 fb^{-1}$ of Monte Carlo simulated data generated using Belle-II software framework. Belle-II experiment is the successor of the Belle experiment at the KEKB accelerator facility in Tsukuba, Japan. It has been designed to make precise measurements of weak interaction parameters and find new physics beyond the standard model. We measure the mass difference (ΔM) between the D^{*0} and D^0 mesons using simulated data. We also calculate the signal yield and reconstruction efficiencies which are crucial inputs for the measurement of the absolute branching ratio of this decay mode using actual data taken by the Belle-II detector.

Contents

1 Introduction

1.1 Elementary particles and fundamental interactions

Particles which do not have any substructure are referred to as 'Elementary Particles'. In other words, these are objects which are not made up of smaller objects. It can be said that the elementary particles are the fundamental constituents of all objects in the universe. Particles can be broadly classified into fermions and bosons based on their intrinsic angular momentum or spin. We first discuss about elementary fermions.

In 1897, the electron (e^-) was discovered by J.J Thomson and it goes back longer into history than any other particle which is considered elementary even now[1]. In 1937, a heavier cousin of the electron was observed, the muon (μ^-).The only difference between the electron and the muon is that the muon is heaver. Rest all properties including charge, spin, etc. are all similar for both the particles. In 1975, another heavier cousin of the electron was discovered, the tau (τ^-). It had more mass than muons as well. All other properties of τ^- were observed to be same as e^- and μ^-, except the mass.

In 1930, in order to explain the continuous spectrum of electrons in nuclear beta decay, Pauli proposed that a neutral fermion was produced in such processes. Neutral fermions are collectively called neutrinos. Pauli's conjecture was proved in 1956, and thus the existence of one kind of neutrinos was confirmed. In the modern terminology, these are called the electron-neutrinos (ν_e) since they are related to beta decay, where an electron is emitted. In the 1960s, it was realized that the muon is also accompanied by its own neutrino, which is now called the muon-neutrino (ν_μ). The tau particle is also believed to have its own neutrino which is different from ν_e and ν_μ, and is denoted by (ν_τ) .These neutrinos, along with the electron, the muon and the tau, form a class of elementary particles which are called leptons. These six leptons, namely the electron and electron-neutrino, the muon and muon-neutrino, tau and tau-neutrino are classified according to certain quantities like charge(Q), electron number (L_e), muon number (L_μ) and tau number (L_τ). They naturally fall into three generations or families as shown in the Table 1. Now, it is known that atleast any particle having a charge has a corresponding anti-particle having opposite charge. Positron is the anti-particle of the electron, anti-muon is the anti-particle of the muon and anti-tau is the anti-particle of the tau. All neutrinos also have corresponding anti-particles referred to as anti-neutrinos. So all the 6 particles in the Table 1, along with their anti-particles which will have all of the quantities in Table 1 with a change of sign, concludes the list of leptons.

Generation	lepton	Q	L_e	L_μ	L_τ
First	e	-1	1	0	0
	ν_e	0	1	0	0
Second	μ	-1	0	1	0
	ν_μ	0	0	1	0
Third	τ	-1	0	0	1
	ν_τ	0	0	0	1

Table 1: Generations of Leptons

Now we look at another class of elementary particles called quarks. Unlike leptons, quarks dont exist in free state. Only bound states of quarks can be observed. Bound states of quarks are called hadrons. For example, protons and neutrons are bound states of quarks and hence are hadrons(Baryons to be exact, will be discussed later). Quarks come in six flavors or types[2]: up(u), down(d), charm(c), strange(s), top(t), bottom(b). These quarks also follow the generational structure: Up and down fall in the first generation, charm and strange fall in the second generation, top and bottom fall in the third generation. The six "flavors" of quarks, can be classified according to charge(Q), strangeness(S), charm(C), bottomness(B), topness(T), upness(U) and downness(D).(Although the last two are seldom used). The classification of the six flavours of quarks along with their generational structure is shown in Table 2. I is isospin, I_3 is third component of isospin. All of these six quarks have anti-particle counterparts called anti-quarks.

Generation	quark	Q	D	U	S	C	B	T	I	I_3	Baryon no.
First	u	2/3	0	1	0	0	0	0	1/2	1/2	1/3
	d	-1/3	-1	0	0	0	0	0	1/2	-1/2	1/3
second	c	2/3	0	0	0	1	0	0	0	0	1/3
	s	-1/3	0	0	-1	0	0	0	0	0	1/3
Third	t	2/3	0	0	0	0	0	1	0	0	1/3
	b	-1/3	0	0	0	0	-1	0	0	0	1/3

Table 2: Generations of Quarks

For anti-quarks, the sign of all these quantities mentioned in the Table 2 will be reversed. The three generations of leptons along with the three generations of quarks along with all their anti-particles, exhaust the list of elementary fermions as it is known today.

Bound states of quarks are called hadrons. Bound state of a quark and an anti-quark is known as a meson and the bound states of three quarks are called baryons (bound states of three anti-quarks are called anti-baryons). The spin of mesons can be zero or one since quarks are spin-1/2 particles whereas baryons can have spin-1/2 or spin-3/2. All quantum numbers defined for quarks in Table 2 are additive. So all quantum numbers in Table 2 can be defined for hadrons as well. For example, baryon number for baryons would be one and for mesons would be zero.

Lets now discuss about fundamental interactions.There are four kinds of fundamental interactions. The oldest known one is the gravitational interaction, known since the time of Newton in the 17th century. In the 19th century, electricity and magnetism were unified into the electromagnetic theory, and this is the second kind of interaction that we recognize to be fundamental. In the early part of the 20th century, with the discovery of the atomic nucleus, it was necessary to introduce two more kinds of fundamental interactions. One of them is the strong interaction, required to explain the stability of the atomic nuclei despite the fact that the protons in the nuclei exert repulsive Coulomb forces on one another. The other is the weak interaction, needed to explain the phenomenon of beta radioactivity, in which an electron or a positron comes out of a nucleus. Among these, gravitational interaction is not included in the standard model as there is no universally accepted quantum theory of gravitation. The gravitational interaction between elementary particles is much feebler than all other interactions. For example, the gravitational potential between two protons is roughly 10^{39} times weaker than the Coulomb potential between them.

In quantum theory interactions occur by exchange of particles. Elementary bosons are these mediators of fundamental interactions. Photons having spin-1 are the mediators of electromagnetic interaction. Gluons (spin-1) are mediators of strong interaction, they are eight in number. Charged W^- and W^+ and neutral Z are mediators of weak interaction (all have spin-1). In addition to this,

Spin	Name	Number	Symbol
1	Photon	1	γ
	W bosons	2	W^+, W^-
	Z boson	1	Z
	Gluons	8	g
0	Higgs boson	1	H

Table 3: Elementary Bosons

electroweak theory postulates the existence of another spinless bosonic particle, called the Higgs Boson, which is responsible for giving mass to all the other elementary particles. Its existence was verified in 2012. Table 3 lists the elementary bosons as observed till date.

1.2 The decay channel

The reconstruction and analysis of the decay:

$$D^{*0} \to D^0\ \pi^0,\ D^0 \to K^-\pi^+, \pi^0 \to \gamma\gamma$$

in Belle-II software framework has been discussed. Generic Monte-Carlo samples were used for this purpose. The final aim is to measure the mass difference of the final state particles which are D^{*0} and D^0 and to measure the branching ratio $\Gamma(D^{*0} \to D^0\ \pi^0)/\Gamma(D^{*0} \to D^0\ \gamma)$ using simulated data (simulated on the basis of the standard model). The signal selection efficiencies and the signal yield obtained in this analysis are crucial inputs for the measurement of the above branching ratio using the actual data taken by the Belle-II detector. This is the first time an analysis of this particular decay mode is being done in Belle-II experiment.

1.2.1 Particles of interest

Before beginning any discussion about the reconstruction and analysis, lets first look at the particles involved in our decay mode[1]. We will first talk about the final state particles which are the ones that are directly detected by the various sub-detectors present in the Belle-II detector owing to their relatively larger lifetimes.

Photons (γ): We first talk about photons. The π^0 particle decays into two photons in our decay mode. Photons are chargeless and massless spin-1 particles which are directly detected by the EM Calorimeter sub-detector of Belle-II.

Kaons ($K^{\pm}$): They are pseudo-scalar strange mesons having iso-spin as 1/2 and spin-parity as (0^-). K^+ and K^- are anti-particles to each other having opposite charges. Quark content of K^+ is $(u\bar{s})$ and that of K^- is $(\bar{u}s)$. The presence of the anti-strange anti-quark in K^+ and strange quark in K^- gives a non zero strangeness value to these mesons. Strangeness(S) of K^+ is 1 and for K^- it is -1. The currently accepted measured mass of these mesons in natural units is 493.677 ± 0.016 MeV. The currently accepted measured mass difference($m_{K^+} - m_{K^-}$) between K^+ and K^- is -0.03 ± 0.09 MeV. The measured mean life of these particles is $(1.2380 \pm 0020) \times 10^{-8} s$.

[1] Information of all particles and branching ratios mentioned has been taken from PDG[3]

Pions $\pi^+ and\ \pi^0$: Both of these are light unflavoured mesons. Their iso-spin value is 1 and their spin-parity is (0^-), making them also pseudo-scalar mesons. π^+ is a bound state of $(u\bar{d})$ and π^0 is a bound state of $(u\bar{u} - d\bar{d})/\sqrt{2}$. Third component of iso-spin (I_3) of π^+ is 1 and that of π^0 is 0. The currently accepted measured mass of π^+ is 139.57039 ± 0.00018 MeV in natural units and its mean life is $(2.6033 \pm 0.0005) \times 10^{-8}$s. The currently accepted measured mass of π^0 is 134.9768 ± 0.0005 MeV and its mean life is $(8.43 \pm 0.13) \times 10^{-17}$s. It is due to this very short lifetime of π^0 that it cannot be detected directly by any sub-detector. Also it is chargeless, so it also does not leave any track in the tracking sub-detectors which are closest to the interaction point. Hence π^0 needs to be effectively reconstructed from the signals of its daughter particles which in our decay mode are photons. The measured mass difference between $\pi^\pm$ and π^0 is 4.5936 ± 0.0005 MeV.

D^0 This is a charmed meson having iso-spin 1/2 and spin-parity (0^-), thus it is a pseudo-scalar meson. It is a bound state of $(c\bar{u})$ having a mass of 1864.84 ± 0.05 MeV and mean lifetime of $(4.101 \pm 0.015) \times 10^{-13}$s.

D^{*0} This is also a charmed meson having iso-spin 1/2 and spin-parity (1^-), thus it is a vector meson. It is also a bound state of $(c\bar{u})$ having a mass of 2006.85 ± 0.05 MeV. Its width is measured to be < 2.1 MeV with a confidence level of 90%.

D^{*0} can decay via two decay modes. The decay modes with their branching fractions are given in table 4.

Mode	Branching fraction $(\Gamma_i/\Gamma_{total})$
$D^{*0} \rightarrow D^0\pi^0$	(64.7±0.9)%
$D^{*0} \rightarrow D^0\gamma$	(35.3±0.9)%

Table 4: Decay modes of D^{*0}

1.2.2 Motivation

The Belle-II experiment is an asymmetric B-factory experiment where electrons (e^-) and positrons (e^+) having 7 and 4 GeV of energy respectively are collided which results in the formation of $\Upsilon(4S)$ resonance at a centre of mass energy of 10.5 GeV. This $\Upsilon(4S)$ then further decays to form $b\bar{b}$ pairs. There is also another less probable possibility where the asymmetric electrons and positrons annihilate to form a photon (γ). This photon produces a $c\bar{c}$ pair. After partial reconstruction of c from this $c\bar{c}$ pair, it combines with a $\bar{u}$ quark to give rise to bound states of $c\bar{u}$. D^{*0} is a bound state of $c\bar{u}$ and hence its production is rare in B-factories.

The decay $D^{*0} \to D^0\pi^0$, is not iso-spin violating and is therefore not suppressed. In the framework of quantum chromodynamics (QCD), coloured quarks interact with each other with the exchange of SU(3) Yang-Mills gauge bosons and also coloured gluons. As a consequence, the quark-gluon dynamics becomes non-perturbative in the low energy regime. To deal with these non-perturbative effects, many effective models like potential model,heavy quark and chiral symmetries, and QCD sum rules have been developed as described in a review[4]. The charmed meson which is described as a hydrogen like hadronic system, consists of heavy quarks (c) and a light quark (u,d,s). Their decays are very well suited to test the effective models mentioned above. The hadronic decay $D^{*0} \to D^0\pi^0$ and the radiative decay $D^{*0} \to D^0\gamma$ have been studied a number of times using the effective models[5]–[8]. A precise measurement of the branching ratio of the above two decay modes will improve these effective models. The branching ratio of D^{*0}: $\Gamma(D^{*0} \to D^0\pi^0)/\Gamma(D^{*0} \to D^0\ \gamma)$ has been measured before by BESIII (2015)[9] and BABAR (2005)[10] experiments at $482pb^{-1}$ and $90.4fb^{-1}$ of integrated luminosity respectively. Their results are:

$$BESIII : 1.90 \pm 0.07(stat.) \pm 0.05(syst.)$$

$$BABAR : 1.74 \pm 0.02(stat.) \pm 0.13(syst.)$$

These experimental results are old now and were performed with low values of integrated luminosity which is the number of events per unit cross section. Further, this decay has not been studied in Belle-II experiment yet. Our aim is to measure new and more precise value for this branching ratio using Belle-II data of $100fb^{-1}$ of integrated luminosity. Higher luminosity means more data which is expected to give more precise results.In order to work on data, we first need to work on simulated monte carlo samples to fix our signal selection efficiencies and to get an idea of the signal yield which is expected while working on data.

Here, we complete the analysis of this decay mode using simulated data of $100fb^{-1}$ integrated luminosity. In addition to that, we also use this simulated data to measure the mass difference of the final state particles (D^{*0} and D^0) and the relative branching ratio $\Gamma(D^{*0} \to D^0\pi^0)/\Gamma(D^{*0} \to D^0\ \gamma)$.

2 The Belle-II Experiment

The Belle-II experiment is an intensity frontier particle physics experiment designed to study primarily the properties of B mesons. However, it also records data for studying properties of charmed and strange mesons as well. It is a part of the SuperKEKB accelerator which is designed to collide electrons and positrons at asymmetric energies of 7GeV and 4GeV respectively. This asymmetry allows for time-dependent charge-parity (CP) symmetry violation measurements. The electron and positron beam collide to produce an $\Upsilon(4S)$ resonance which decays to produce $b\bar{b}$ pairs. Hence it is known as a B-factory. The design luminosity of SuperKEKB is $8 \times 10^{35} cm^{-2} s^{-1}$ which is 80 times larger than its predecessor's (KEKB) design luminosity and 40 times its recorded peak luminosity. With this large luminosity, this experiment is expected to produce 5×10^{35} b,c and τ pairs in a period of eight years. All technical information about the Belle-II detection in the next section have been taken from the Belle-II technical design report[11].

2.1 The Belle-II detector

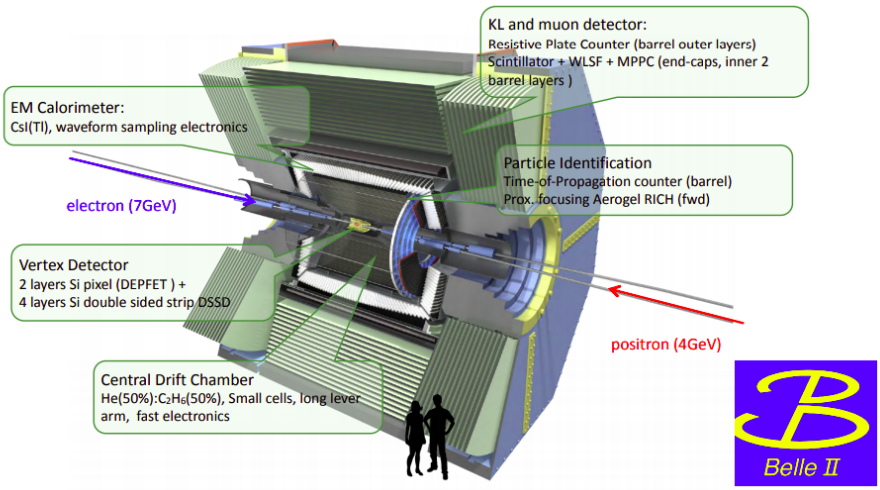

Figure 1: The Belle-II detector

Figure 1[1] shows the various components and sub-detectors of the Belle-II detector

[1]image source: Matvienko, D. The Belle II experiment: status and physics program[12]

The Belle-II detector can be subdivided into five sub-detectors. Each of them have different detection mechanisms to detect specific particles.

Vertex Detector (VXD): Vertex detectors are used to precisely measure the angles and positions of charged particle tracks so as to differentiate tracks originating from decay vertices from those originating from the interaction point. The VXD consists of two components, the Pixel Detector (PXD) having two consequtive cylindrically symmetric layers around the beam pipe and the Silicon Vertex Detector (SVD) having four layers around the beam pipe (10 mm radus). So in total there are six layers around the beam pipe which form the Vertex Detector in Belle-II.

The first two layers around the beam pipe are the Pixel detectors (PXD) at radius of 14 mm and 22 mm which use pixelated DEPFET (Depleted Field effect Transistors) sensors.

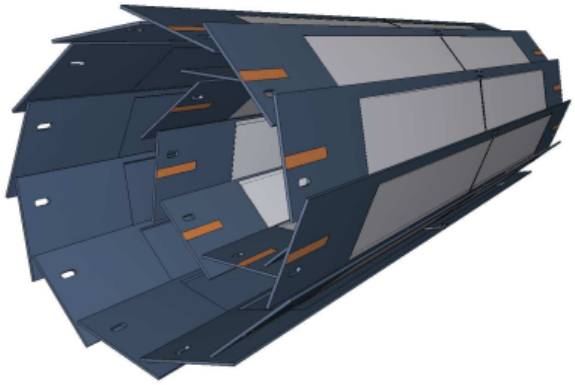

Figure 2: Two layers of PXD

Figure 2[1] shows a schematic view of the layout of the pixelated sensors in the PXD layers. The grey region comprises of the DEPFET sensors which are 50 μm thin. A total of 40 pixel sensors are cylindrically arranged in the two layers of PXD. The outer layers are 174 mm covering the entire acceptance of the tracker system. When charged particles pass through the semiconducting pixel sensors, electron and hole pairs are produced which traverse to the positive and negative electrodes attached to the sensors thereby producing a signal. This signal is detected by readout channels which are present for each of the pixelated sensors on the two layers of PXD. By investigating which sensors got activated in both layers, one can reconstruct a track for the charged particles that had passed through the detectors.

[1]Image source: Belle-II technical design report[11]

layer	Radius (mm)	Ladders	DSSD's/ladder
L6	140	17	5
L5	115	14	4
L4	80	10	3
L3	38	8	2

Table 5: Arrangement of SVD detector

The next four layers of VXD present at a radius of 38 mm, 80 mm, 115 mm, 140 mm from the beam pipe consists of double sided silicon strip sensors (DSSD) which makes up the Silicon Vertex Detector (SVD). These four layers of the Silicon Vertex detector are subdivided into ladders and each ladder consists of a fixed number of sensors. Table 5 gives information of the number of ladders present in the four layers of the SVD sub-detector and the number of sensors present in each ladder. The layers have been numbered from 3 to 6 as there are two layers of VXD before the SVD sub-detector around the beam pipe.

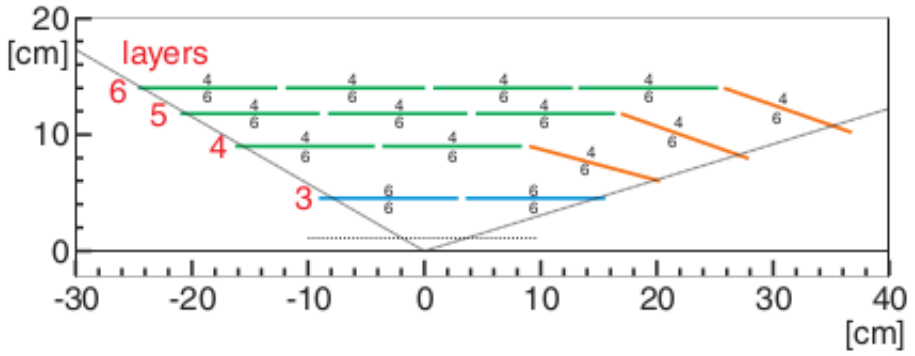

Figure 3: Scehematic diagram of different sensor geometries used in SVD sub-detector

Three types of DSSD's are used in SVD to increase the acceptance of particles. They are trapezoidal, large and small rectangular sensors. In Figure 3[1], the green sensors are large rectangular type, the blue ones are small rectangular type and the orange ones are trapezoidal sensors. The working principle of these sensors are similar to that of the pixel sensors in PXD as both of them are semiconductor detectors. In DSSD, a charged particle

[1]Image source: Belle-II technical design report[11]

passing through the silicon sensor produces electron and hole pairs. These the travel towards the electrodes present in opposite surfaces with opposite polarities which creates a signal which is then measured using readout channels. Each of these electrodes are actually made in form of strips. Strips present on opposite faces of the silicon semiconductor are oriented at an angle of 90 degrees relative to each other. Signal is measured from each of these strips. The relative orientation of 90 degress of the strips on both surfaces provides information of two coordinates. The main aim of SVD along with VXD and CDC (central drift chamber) is the measurement of the vertex for the two B mesons. In addition to this, SVD also measures the vertices in other decays involving D mesons and τ lepton.

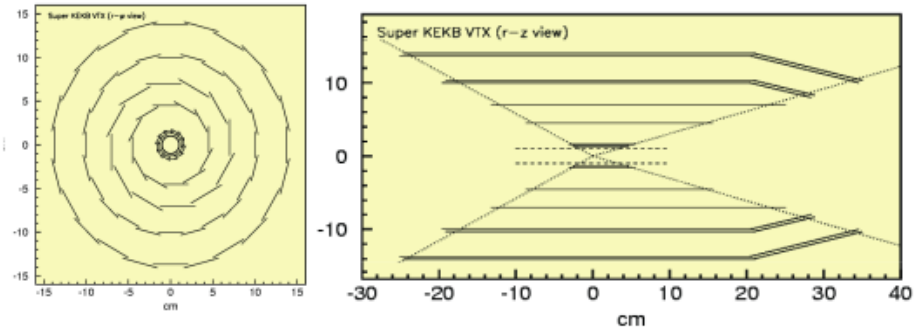

Figure 4: Belle-II vertex detector

Figure 4[1] shows a schematic representation of the vertex detector in Belle-II with two layers of Pixel detectors around the beam pipe and then four layers of silicon vertex detector.

Central Drift Chamber (CDC): Drift Chamber detectors are ionization detectors which provides accurate measurements of the position of charged particles passing through the detector. When a charged particle passes through the gas present in a drift chamber, electromagnetic ionization of the atomic electrons occur which results in the formation of electron-ion pairs. The number of such pairs produced is dependent on the energy of the incident particle. Application of an electric field through positive and negative electrodes, results in the drifting of the electrons towards the positive electrode and the positive ions towards the negative electrode. However the drift velocity of ions is negligible and can be ignored. Electrons which drift through the gas, on reaching near the anode, where the electric field is high, gains enough energy to knock other electrons out of the gas atoms present in the

[1]Image source: Belle-II technical design report[11]

vicinity. These secondary electrons further ionize more electrons thereby creating an avalanche which leads to an exponential increase in the number of electrons near the anode. The large number of electrons when they reach the anode constitutes a measurable current. An electron produced far away from the anode experiences a small electric field. This electron will drift towards the anode with drift velocity proportional to the applied electric field and hence this drift velocity can be measured. When this electron reaches close to the anode, an avalanche process will be initiated by this electron. Now since this electron travels most of the distance with a velocity that is predictable (proportional to the applied electric field), a careful measurement of the time it took to reach the anode after the charged particle was incident on the detector, gives us measurement of the distance from the anode to the point where it was created, i.e the point from where the original source particle had passed. In this way, drift chamber detectors provide measurements of the position of charged particles.

The gas mixture used in the central drift chamber sub-detector of the Belle-II detector is $He - C_2H_6$ 50:50 mixture. The CDC provides efficient signals for charged particles giving precise information of their momenta and position. It also provides for particle identification by measurement of energy loss inside the gas mixture. This is particularly useful because particles having low momentum tracks can be identified using CDC as they might not reach the particle identification (PID) sub-detectors of Belle-II.

Particle Identification PID: PID in Belle-II is achieved through two sub-detectors: Time of propagation (TOP) counter in barrel region and Aerogel Ring Imaging Cherenkov (ARICH) detector. Particle identification is crucial in differentiating Kaons from Pions. It reduces the probability of misidentifying a Kaon for a Pion and vice-versa. Both TOP and ARICH work on the basic principle that when a charged particle passes through a medium with a velocity greater than the velocity of light in that medium, then it emits Cherenkov light at a characteristic angle. This angle depends on the velocity of the particles. Kaons and Pions passing through a PID detector having same momentum will have different velocities (as $p = \gamma mv$) and hence will emit Cherenkov photons at different characteristic angles. In TOP counters, this Cherenkov radiation undergoes total internal reflection. Since the characteristic angles are different for Kaons and Pions, they will travel through different path lenghts and hence will have different time of propagation. Figure 5[1] shows a conceptual overview of the TOP counter.

In the endcap, ARICH consists of an aerogel radiator where Cherenkov pho-

[1] Image source: Belle-II technical design report[11]

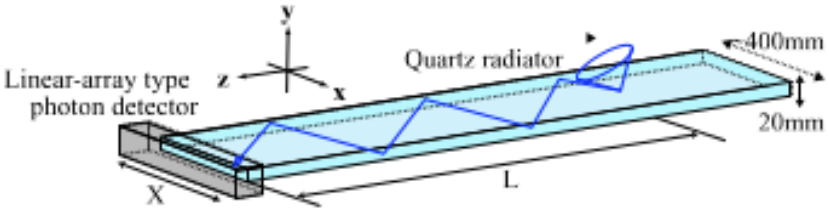

Figure 5: Overview of TOP counter

tons are produced when charged particles are incident on it. An expansion volume is present to allow the produced Cherenkov photons to form rings on the surface of the photon detector. Radius of these rings would be different because of different characteristic angles of the emitted photons. Highly efficient position sensitive photon detectors along with a read-out system is used to detect the Cherenkov photons. A schematic diagram describing the basic working of ARICH is shown in Figure 6[1].

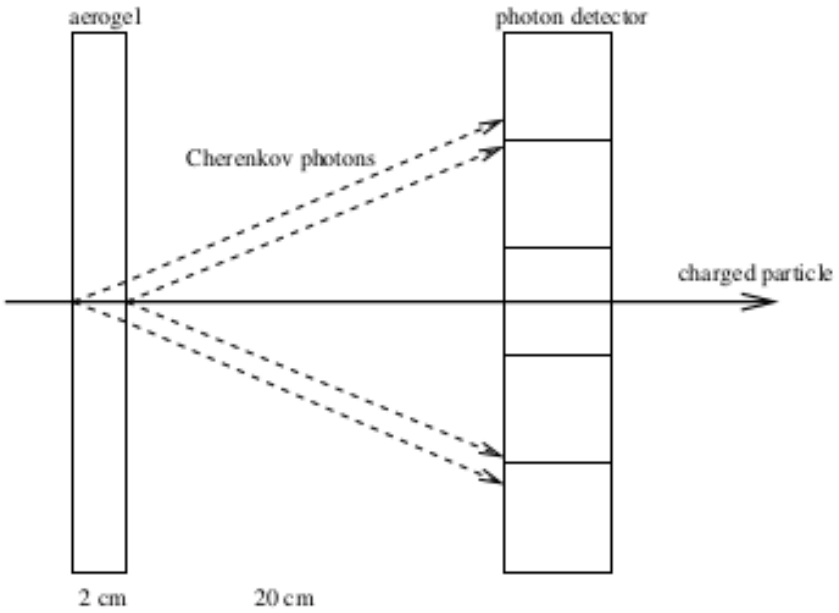

Figure 6: Working of ARICH

Electromagnetic Calorimeter (ECL): Calorimeters are primarily used to detect

[1]Image source: Belle-II technical design report[11]

photons, electrons and hadrons. They are classified into two categories: electromagnetic and hadronic calorimeters. Electromagnetic calorimeters are used for the detection of electrons, photons and also the π^0 mesons as they decay into photons. These calorimeters are blocks of a selected material which absorbs the incident particles. The particles interact with the calorimeter material either electromagnetically (in electromagnetic calorimeter) or through strong interaction (in hadronic calorimeter) to produce showers of secondary particles with decreasing energy. The energy of these secondary particles are deposited in the calorimeter and can be detected in the form of light or charge which can be used to measure the energy of the incident particle. The size of an electromagnetic shower is governed by a single parameter known as the radiation length X_0. It depends on the material of the calorimeter. If an electron travels X_0 distance inside the calorimeter then its energy reduces by a factor of $1/e$. For photons, which are absorbed by the material through pair production, their energy reduces to $1/e$ of their incident energy when they travel a distance of $9/7X_0$ inside the calorimeter.

In Belle-II, the calorimeter is of electromagnetic type which is used for the detection of photons and identification of electrons with high efficiency. Thallium doped Caesium Iodide $CsI(Tl)$ is used as the detector material because it has a relatively shorter radiation length, high mechanical strength, high light output and moderate price. The ECL consists of a 3 m long barrel section with an inner radius of 1.25 m and annular endcaps at z = -1.0 m (backward part) and z = 2.0 m (forward part) from the interaction point. The z axis is taken parallel to the beam pipe. It covers a polar angle region of $12.4^\circ < \theta < 155.1^\circ$ leaving a gap of about 1° between the barrel and endcaps.

K_L^0 and μ detection (KLM): This sub-detector which is located outside the superconducting solenoid consists of alternating layers of 4.7 cm thick iron plates and detector elements (resistive plate chambers). This also has three components, one barrel and two endcaps. The polar angle range of the barrel is $45^\circ < \theta < 125^\circ$ which is extended by the endcaps to $20^\circ < \theta < 155^\circ$. Muons and charged hadrons which do not produce showers in the subdetector (i.e they do not interact hadronically), pass through it (this is dependent on the polar angle of the particle but roughly if their momentum is greater than about 1.5 GeV/c) or loses energy completely due to electromagnetic deposition. K_L mesons interacts in the iron plates of the KLM (also in ECL) producing hadronic showers that can be detected in both ECL or KLM.

The active detector element used in KLM are glass electrode RPC's. Glass

in general is insulating but it does conduct electricity but with very high resistivity of around 5×10^{12} Ωcm. Two parallel sheets of float glass act as electrodes. The composition of these electrodes in barrel and endcap are: 73% silicon dioxide, 14% sodium oxide, 9% calcium oxide and 4% uncategorized compounds for the 2.4 mm thick barrel glass ; 70-74% silicon dioxide, 12-16% silicon oxide, 6-12% calcium oxide, 0-2% aluminium oxide, and 0-4% magnesium oxide for the 2 mm thick endcap glass. These parallel layers of glass sheets are seperated by 1.9 mm thick noryl spacers. In the gap, a gas mixture of 62% HFC-134a, 30% argon, and 8% butane-silver which is a mixture of 70% n-butane and 30% isobutane is used. The basic working principle of RPC's is that when a charged particle passes through it, it ionizes the gas molecules inside creating electron and ion pairs. A trigger system is used to produce a high voltage difference inside the gas cavity which accelerates positive ions towards the cathode and negative electrons towards the anode. This produces a spark in the exact trajectory of the particle. If metallic electrode plates are used, then this spark can discharge the electrode plates and increase its temperature thereby damaging the electrode. Therefore glass electrodes having high resistivity is used to avoid this problem.

Muon identification is substantiated by the KLM. Muon identification begins by reconstructing its charged tracks mainly from CDC. If some muons pass atleast one of the RPC detectors in KLM (when muon momentum is atleast 0.6 GeV/c), then this signal hit in the KLM is added with the track in CDC. This extrapolates each track which provides for more accurate identification of muons. Kaon (K_L) identification is done by studying the clusters formed as a result of hadronic showers formed due to the interaction of the kaons with the iron plates. The signal produced are grouped together to form a cluster. K_L^0 mesons have a long lifetime (5.2×10^{-8}) and they are chargeless and therefore they travel through the entire detector without any interaction in any of the other sub-detectors. Hence, the KLM sub-detector present at the very end is important for their detection and identification.

2.2 The Belle-II software framework

Belle Analysis Software Framework II or Basf2[1] is the successor of the previous framework (Basf) which was used for the Belle detector (predecessor to the Belle-II detector). This software is used mainly for the purpose of selecting final state particles by using detected information of particle trajectories, ECL Clusters, PID likelihoods, etc. These particles are then combined using the 'Analysis' software package pre-defined in the framework to reconstruct the decay chain which is being analyzed by creating mother particles after combining the 4-momentum of its daughter particles. Basf2 is actually used in all aspects of data processing at Belle-II. In this analysis of $D^{*0} \to D^0\pi^0$, the software has been used to reconstruct the decay chain and extract necessary variables which are important to the analysis. It has also been used to classify signal and background for certain variables by a process known as Monte-Carlo (MC) Truth Matching, which will be discussed later.

2.2.1 Core aspects of Basf2

Some of the important core aspects of Basf2 software framework are:

Basf2 modules: A data processing chain in Basf2 consists of small units of data processing which are assigned to do specific tasks. These are called modules which are usually pieces of C++ code used in the analysis to perform tasks like loading input files, creating particles lists etc.

Path: Modules used in an analysis are laid out as an ordered list in a sequence in which the user wants them to be executed. This list is called the path and is executed by the Basf2 software.

Package: These are collection of codes in Basf2 which contains several modules. These can be invoked to import modules which perform similar tasks. for example, there is a module called modularAnalysis which contains modules (member functions of the package) to perform tasks related to analysis like creating final state particle lists, creating mother particle lists by combining daughter particles, etc.

Steering file: This is the actual code that an analyzer writes for a particular analysis. This file would declare a path, set up all necessary modules and add them in order of execution to the path and finally process the path to extract the information that is required for the analysis.

[1] All information in this section has been taken from Belle-II online software documentation[13]

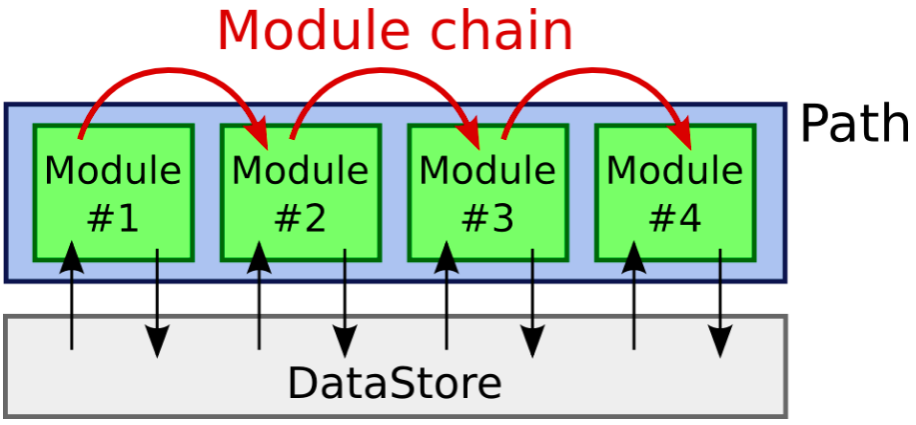

Figure 7: Basf2 processing flow chart

Figure 7[1] shows a schematic diagram of data processing in Basf2. In a steering file, initially necessary packages are imported based on what modules will be used. The modules are then declared and set up to perform the desired task. They are then arranged in a linear order in a path. The data which is to be processed is stored in a common storage called the 'DataStore'. Each module has read and write access to it. The path is then processed. The framework then executes the modules defined in the path sequentially one after the other from first till the end.

2.2.2 Data file formats

The particles formed as a result of the electron and positron beam collision in the Belle-II detector are detected by the sub-detectors. The raw data generated is saved to a disk in binary format after signal from all sub-detectors are matched in time as each sub-detector has different response times. This raw data is hardly of any direct use in any physics analysis. They are subjected to several processes like unpacking, calibration, reconstruction and are converted to files which can be used to generate a physics result. There are four kinds of data objects which are stored in four kinds of files respectively:

raw objects: These are the raw output from the sub-detectors which needs further processing in order to do a physics analysis. These data objects are stored in what are known as 'RAW' files.

low-level objects: After the first data processing step in RAW files, which is unpacking them, low level objects are formed and they are stored in cDST

[1] image source: Belle-II confluence page[14]

(calibration Data Summary Table) files. These files are important in studying the performance of the detector, but they are not useful for any analysis.

reconstruction-level objects: The reconstruction converts low-level data objects of cDST files to high-level variables like ECL clusters, PID likelihoods, particle trajectories, impact parameter variables etc. These high-level objects are stored in mDST (mini Data Summary Table) files. These mDST files are used in all physics analysis as they can be used to extract the necessary variables of particles in a decay mode that is being studied..

analysis-level object: These objects are stored in uDST (user Data Summary Table). This is a result of a skimming procedure performed on mDST files which selects the specific events that are relevant for a particular physics analysis. These files contain information in terms of variables for the particles that are present in the decay chain that is being analyzed.

In the analysis of $D^{*0} \to D^0\pi^0$, mDST files have been used as an input to the steering file which was written to select the final state particles, reconstruct the mother particles from the final state particles and also to extract variables needed to perform the analysis.

All these files, mentioned above are ROOT files, i.e they are of .root format. The output of the steering script is also of .root format. They are analyzed using the open source software called ROOT, developed by CERN. This software allows us to do a wide range of tasks like plotting histograms, generating graphs, and much more.

2.2.3 Important packages and modules:

Packages and modules that were used in the steering script for the present analysis has been mentioned in this section.

basf2: This package was used to create and process the execution path were modules were stored and later processed. create_path() and process() member functions were used to create and process the path respectively.

modularAnalysis: This is the most important package as several modules of this package has been used in the analysis.

inputMdstList() was used to load the input files (mDST files) for the analysis. Generic Monte-Carlo samples were used as input for this analysis.

fillParticleList() is used to select final state particles which are detected by the detector. This module creates the required particles from the corresponding high level data objects present in the input mDST file based on the

selection criteria provided to it as argument (for example charged particles are created from track objects and photons are created from ECL Cluster objects in the mDST files). The charge conjugated particle lists of a desired particle is also created by default.

reconstructDecay() is used to create new particles by combining the final state particles via a specified decay mode. All possible combinations of the daughter particles are produced but the ones which satisfies the selection criteria given as an argument to this function are stored in a new mother particle list. By default, the charge conjugated decay is also reconstructed and hence a particle list for the charge conjugated mother is also created.

matchMCTruth() is used to match the created particle lists with MC Particle lists. The input files used for the current analysis are generic Monte Carlo samples. They contain simulated events generated by an event generator (very similar to actual data). During event generation of all possible decays, MC Particle lists are created. A match result of the selected particle lists and MC Particle lists, enables us to distinguish between signal and background. Each particle, i.e all daughters and the mother particles are truth matched to identify whether the selected daughter particles are coming from the reconstructed mother particle. MC truth matching generates three variables: isSignal, mcErrors, isPDG. In the present analysis, the variable of interest is isSignal. Truth matching is performed for every entries and for entries where the mother particle is correctly reconstructed, isSignal variable value returns 1 else 0. The entries where isSignal value of a particular particle is 1 will represent signal and the entries where this value is 0 will represent background.

variablesToNtuple() is used to create and fill ntuples with values of specified variables for each entry of the input file in an output .root file.

vertex: Vertex fitting is the process of using prior knowledge of a particular decay to improve the measurement of its observables. There are two types of vertex fitting: geometric and kinematic fitting. Geometric fitting is used to determine the decay vertex of a particle by fitting together the tracks of its charged decay daughter particles which are known to originate from a common point. Kinematic fitting is used for better measurement of particle kinematics. The composite particles are reconstructed from its daughters through 4-momentum conservation. Now if it is known from prior knowledge that this particle has a well defined mass, then it is beneficial to apply a mass constraint while reconstruction as this reduces combinatorial background.

Vertex is a package which offers a module called kFit() which enables the

user to do three kinds of vertex fitting (normal vertex fit, vertex fit with a mass constraint on the composite particle and a vertex fit with the 4-momentum of the composite particle constrained to the 4-momentum of the beam) and also mass constrained kinematic fit.

variables.collections and variables.utils: variables.collections imports predefined collection of variables which are then assigned to the particles by a module named create_aliases_for_selected() which is the member function of variables.utils.

In the next section, the analysis of the decay mode $D^{*0} \to D^0\pi^0$ has been discussed.

3 Analysis of $D^{*0} \to D^0\pi^0$

In this analysis, generic Monte Carlo (MC14 run independent samples) of 100 fb^{-1} available in KEKCC (KEK Computing Centre) were used as input data files. These are not actual data taken by the detector, but they are very close to the actual data. Any analysis is first done on these MC files to determine proper selection criteria for the particles and proper signal selection efficiency of the decay, and then actual data is used. Basf2 was used for the reconstruction of the decay chain:

$$D^{*0} \to D^0\ \pi^0,\ D^0 \to K^-\pi^+,\ \pi^0 \to \gamma\gamma$$

Optimization of discriminating variables was done in order to reduce background. Optimized mass difference variable ($\Delta M(m_{D^{*0}} - m_{D^0})$) was fitted to obtain the measured value of this mass difference from simulated data. The reconstruction of the decay chain mentioned above has been discussed in the following subsection.

3.1 Reconstruction

In order to begin the reconstruction of any decay mode, some loose pre-selection criteria needs to be specified. These are known as pre-selection cuts.

3.1.1 Pre-selection cuts

Pre-selection cuts are a starting point of any analysis. These are generally based on the analysis of similar decay modes at a particular experiment which here is Belle-II. Internal Belle-II notes[15][16] of previous analysis involving similar decay modes were studied and suitable pre-selection cuts were chosen.

K^- and π^+ are the final state charged particles in this decay chain. Loose selection cuts on charged particle tracks and particle ID has been used to fill data in particle lists for the kaons and the pions. For cuts on tracks, selection criteria was imposed on the radial distance (dr) and the axial distance (dz) of the point of closest approach (POCA) of the tracks from the interaction point. Chosen pre-selection on these variables:

$$dr < 0.5cm \text{ and } |dz| < 2cm$$

Since Kaons and Pions have a tendency to fake as each other during their detection, it is crucial that a selection criteria is used to distinguish them using Particle Identification variables. The variables used are dual KaonID and dual PionID defined as $kaonID = L_K/(L_K + L_\pi)$ and $pionID = L_\pi/(L_K + L_\pi)$. A loose criteria was imposed on these variables which loosely distinguishes Pions and Kaons, in order to begin the reconstruction. Selection cut used:

$$kaonID = L_K/(L_K + L_\pi) > 0.3,\ pionID = L_\pi/(L_K + L_\pi) > 0.3$$

where L_K and L_π are likelihoods of detecting kaons and Pions by the detector.

Selection criteria on the energy of the photons (γ) as detected in the three regions of the electromagnetic calorimeter has been used to select the photons present in the decay chain. These cuts are based on previous analysis of other decay modes studied in Belle-II involving a π^0 going to two γ's. The selection cuts used:

$$E_\gamma^{barrel} > 30\ MeV,\ E_\gamma^{forward} > 120\ MeV,\ E_\gamma^{backward} > 80\ MeV$$

. For photons, in addition to selection criteria on their energy, cuts were also applied on the number of activated crystals inside the cluster of the electromagnetic calorimeter, the energy ratio of the energy deposited on the central crystal to the energy deposited on nine crystals around the central crystal (E1/E9) and the cluster's polar angle (θ).

In basf2, the variable 'clusterNHits' returns the sum of weights w_i ($w_i \leq 1$) of all crystals in an electromagnetic cluster. If the clusters are non-overlapping, this is equal to the number of crystals in the cluster. If the energy splits among nearby clusters, this can be a non integer value. 'clusterTheta' or θ returns the polar angle of the electromagnetic cluster. The direction of the cluster is given by a line joining the interaction point and the cluster centroid position. The energy ratio of the energy deposited on the central crystal to the energy deposited on nine crystals around the central crystal is (E1/E9) and the variable in basf2 is 'clusterE1E9'. The pre-selection on these variable are:

$$clusterNHits > 1.5,\ 0.2967 < clusterTheta < 2.6180,\ clusterE1E9 > 0.4$$

For π^0, a cut on its mass has been applied in addition to a mass constrained kinematic fit to reduce combinatorial backgrounds. From section 1.2.1, $M(\pi^0) \approx 0.135\ GeV/c^2$. Selection cut condition used is:

$$0.127 < M(\pi^0) < 0.139\ GeV/c^2$$

For D^0 meson, a selection criteria on its mass of all possible resonances of $K^-\pi^+$ was incorporated. From section 1.2.1, $M(D^0) \approx 1.86\ GeV/c^2$. The selection cut used to fill particle list for this meson:

$$1.70 < M(K^-\pi^+) < 2.05\ GeV/c^2$$

And finally for the initial particle, which is D^{*0}, a cut on its centre of mass frame momentum has been used to extract events resulting due to $c\bar{c}$ production after the electron and positron beams collide. These events are jet like events where the momentum of the resonance particles formed is high in comparision to resonances formed through $b\bar{b}$ pairs where the particles formed are almost at

rest. In addition to this, mass difference between the D^{*0} and D^0 has been used to tag this particle. The measured value of this mass difference is [1] $m_{D^{*0}} - m_{D^0} = 142.014 \pm 0.030\ MeV$. Selection cuts used:

$$p_{COM}(D^{*0}) > 2.5\ GeV/c$$

$$0.058 < m_{D^{*0}} - m_{D^0} < 0.194\ GeV/c^2$$

The reconstruction of this decay chain was done in Basf2 which will be discussed in the following section.

3.1.2 Reconstruction using Basf2

The full decay chain was totally reconstructed using Basf2. Necessary variables including the kinematic variables for the all particles which would be used in optimization and MC truth match variable isSignal for D^{*0} were extracted and saved.

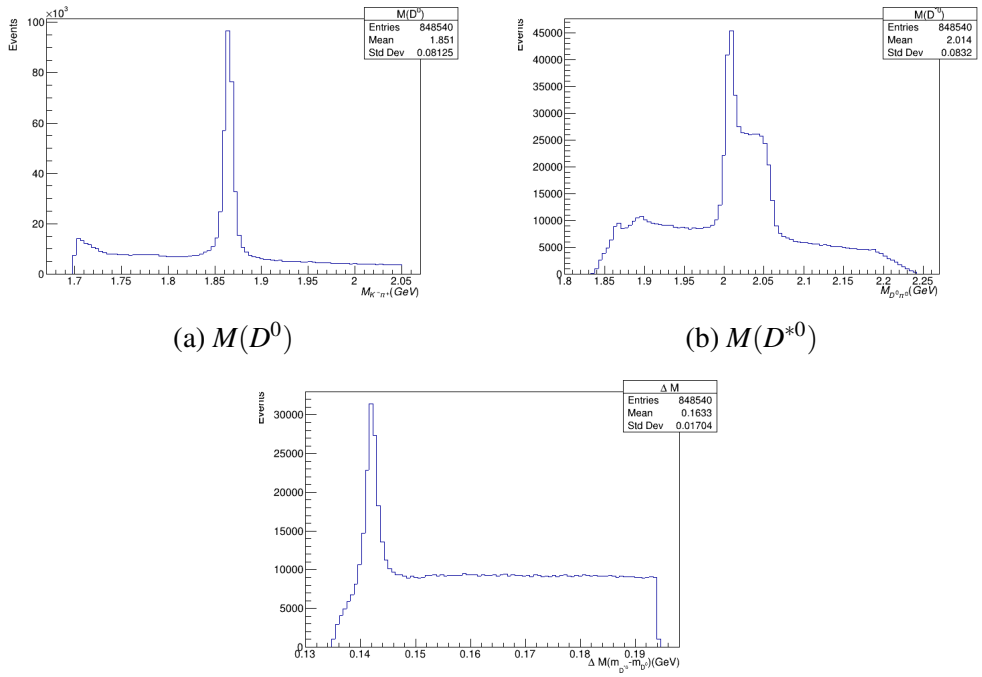

(a) $M(D^0)$

(b) $M(D^{*0})$

(c) $\Delta M(m_{D^{*0}} - m_{D^0})$

Figure 8: Mass and mass difference distributions

[1] Value taken from PDG

Figure 8(a) shows the mass distribution of D^0 meson after reconstruction with pre-selection cuts. The mean of the distribution is $\approx 1.85 GeV/c^2$ which is in good agreement with the expected mass of D^0 which is about $\approx 1.86 GeV/c^2$. Figure 8(b) shows the mass distribution of D^{*0} meson, which is the ultimate final state particle in the decay chain. The mean of the distribution ($\approx 2.01 GeV/c^2$) is also in very good agreement with the expected mass of D^{*0} which is also about $\approx 2.01 GeV/c^2$.

Mass difference variables serve as very effective tagging tools for heavy mesons like D^{*0} which have well defined mass difference values with their heavy decay product which here is D^0. The currently accepted measured value of this mass difference is [1] $\Delta M(m_{D^{*0}} - m_{D^0}) = 142.014 \pm 0.030\ MeV/c^2$. Figure 8(c) shows the mass difference after reconstruction. There is a peak around the expected value of this mass difference.

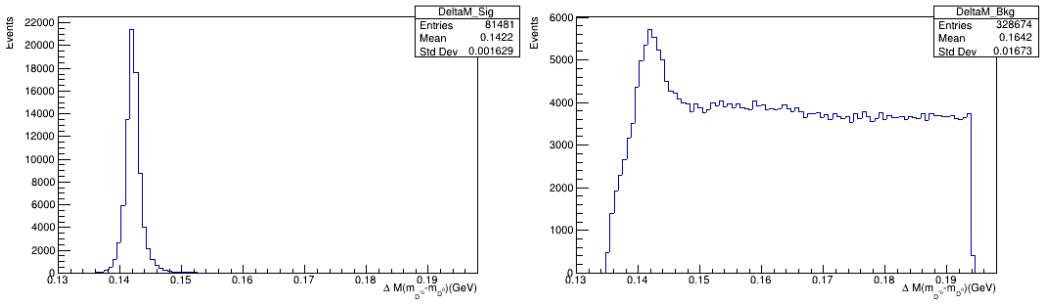

(a) Signal for ΔM (isSignal = 1) (b) Background for ΔM (isSignal = 0)

Figure 9

Using MC Truth match variable isSignal, the signal and background components of the distribution in Figure 8(c) has been separated. The mean of the signal distribution in Figure 9(a) is $\approx 0.142 GeV/c^2$ which is in very close agreement with the expected value of the mass difference. Hence we can say that the decay chain has been reconstructed successfully.

Figure 10 shows the stacked signal and background for the distributions in Figure 8. These figures gives a better visualization of the signal and background components in the mass and mass difference distributions. From these figures, it is evident that there is a peaking backround around the signal region in all the three distributions along with a combinatorial background. Optimization needs to be

[1] Value taken from PDG

done so as to reduce these backgrounds and to gain clean access of the signal. This should decrease both the peaking and the combinatorial backgrounds. The prime variable for the analysis, which is the mass difference variable will be primarily investigated during optimization.

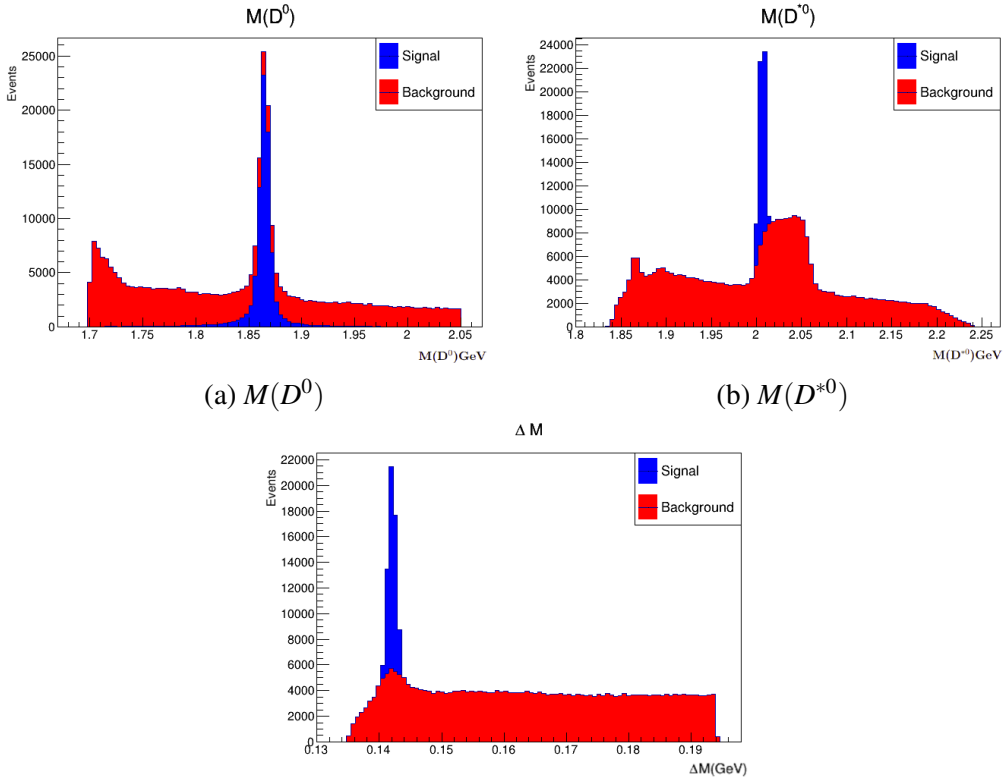

(a) $M(D^0)$ (b) $M(D^{*0})$

(c) $\Delta M(m_{D^{*0}} - m_{D^0})$

Figure 10: Signal and background components of mass and mass difference distributions

If the peaking background is present even after the optimization then that needs to be investigated separately to have an idea of decay modes which contribute to the peaking background.

In the subsequent section, optimization using 'cut and count' method would be discussed.

3.2 Optimization using Cut and Count

The process of reducing background by optimizing the selection cuts used for different parameters or to include new parameters and impose suitable selection cuts on them is called optimization. In this analysis, the 'cut and count' method of optimization have been used.

In the cut and count method, after a variable or parameter has been selected for optimization, the entire range of values, for which both the parameter's signal and background show a distribution, is subdivided into small intervals. The value of the variable after each such interval is a probable cut value. For each of these probable cut values, the number of signal and background events that would remain after incorporating the cut is computed. Then a parameter called figure of merit (FOM) is calculated for each of these probable cut values, which is given by:

$$FOM = \frac{\varepsilon_s}{\sqrt{N_b}},\ where\ \varepsilon_s = \frac{Number\ of\ signal\ events\ after\ the\ cut}{Initial\ number\ of\ signal\ events\ without\ any\ cut}$$

$$N_b = The\ number\ of\ remaining\ background\ events\ after\ the\ cut$$

ε_s is called the signal selection efficiency and

$$\varepsilon_b = \frac{Number\ of\ background\ events\ after\ the\ cut}{Initial\ number\ of\ background\ events\ without\ any\ cut}$$

is called the background selection efficiency and so $(1-\varepsilon_b)$ is the background rejection efficiency for the particular variable being optimized. After computing FOM, ε_s and ε_b they are plotted for all probable cut values in the range of the variable whose optimization is being done. From this plot, the value of the cut variable is carefully chosen such that higher signal selection and higher background rejection is ensured. Generally the value at which FOM shows a maximum is chosen as it corresponds to the highest signal efficiency with respect to the number of background events after the cut.

Before beginning the optimization, variables need to be chosen which can be optimized to reduce background without much loss of signal. For this purpose, signal and background overlay plots of kinematic variables of all particles present in the decay chain needs to be investigated.

3.2.1 Variable selection for optimization

All variables for all particles which were saved after reconstruction will be investigated to choose strong signal and background discriminating variables for optimization.

D^{*0} variables:

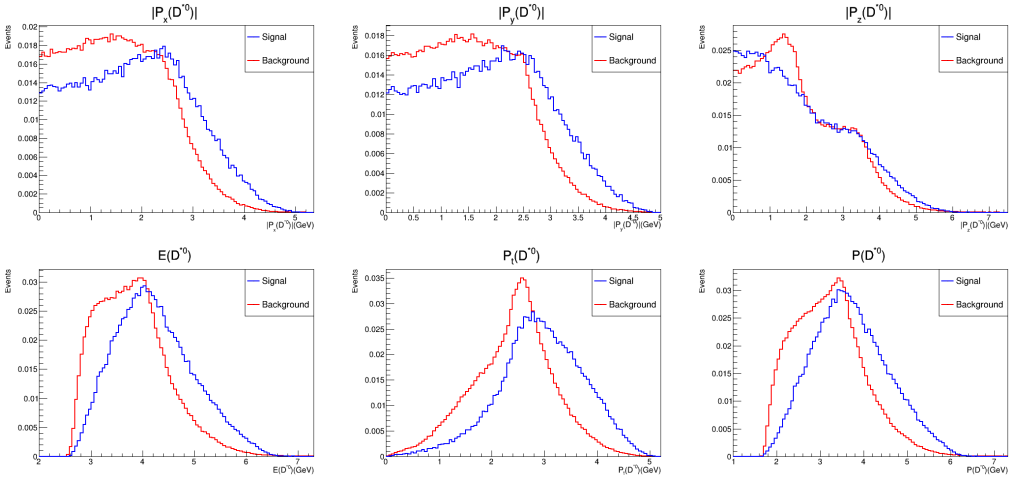

Figure 11: Overlay plots for D^{*0} variables

Figure 11 shows the overlay signal and background distributions for the kinematic variables of the D^{*0} meson which includes the absolute value of the momentum in x,y and z directions and the energy, transverse momentum and magnitude of momentum of the meson.

D^{0} variables:

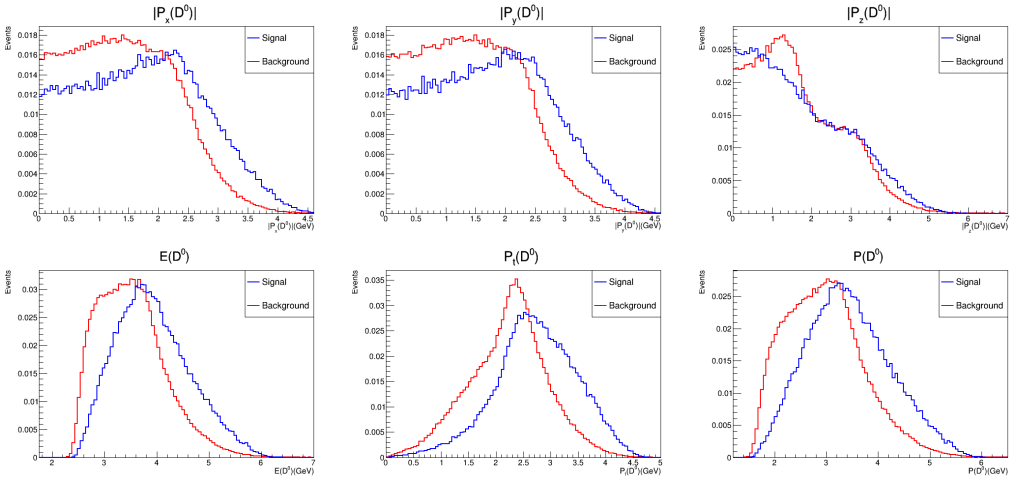

Figure 12: Overlay plots for D^{0} variables

Figure 12 shows the overlay signal and background distributions for the kinematic variables of the D^0 meson which includes the absolute value of the momentum in x,y and z directions and the energy, transverse momentum and magnitude of momentum of the meson (the same variables as there were for D^{*0}).

K^- variables:

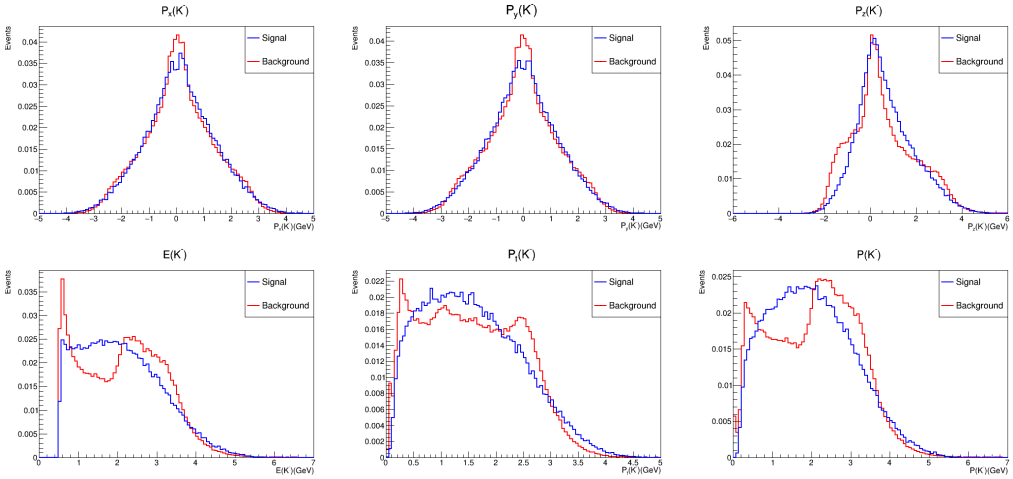

Figure 13: Overlay plots for K^- variables

Figure 13 shows the overlay signal and background distributions for the kinematic variables of the K^- meson which includes the distribution of the momentum in x,y and z directions and the energy, transverse momentum and magnitude of momentum of the meson.

π^+ variables:

Figure 14 shows the overlay signal and background distributions for the kinematic variables of the π^+ meson which includes the distribution of the momentum in x,y and z directions and the energy, transverse momentum and magnitude of momentum of the meson (the same variables as there were for K^-).

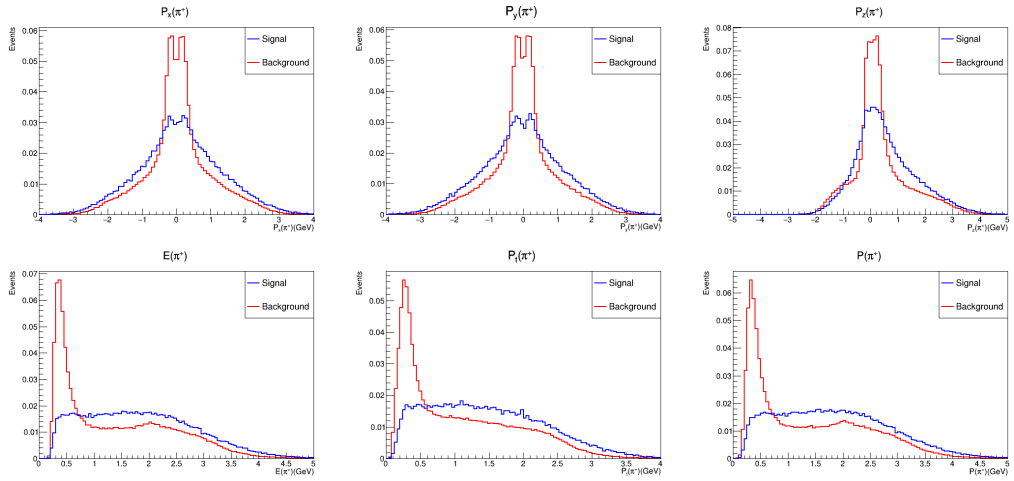

Figure 14: Overlay plots for π^+ variables

π^0 variables:

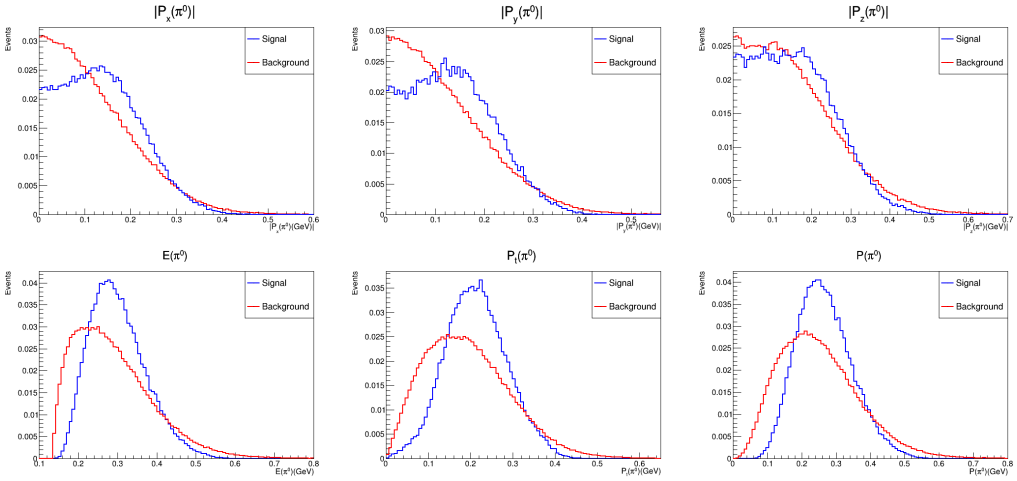

Figure 15: Overlay plots for π^0 variables

Figure 15 shows the overlay signal and background distributions for the kinematic variables of the π^0 meson which includes the distribution of the absolute value of momentum in x,y and z directions and the energy, transverse momentum and magnitude of momentum of the meson.

γ variables:

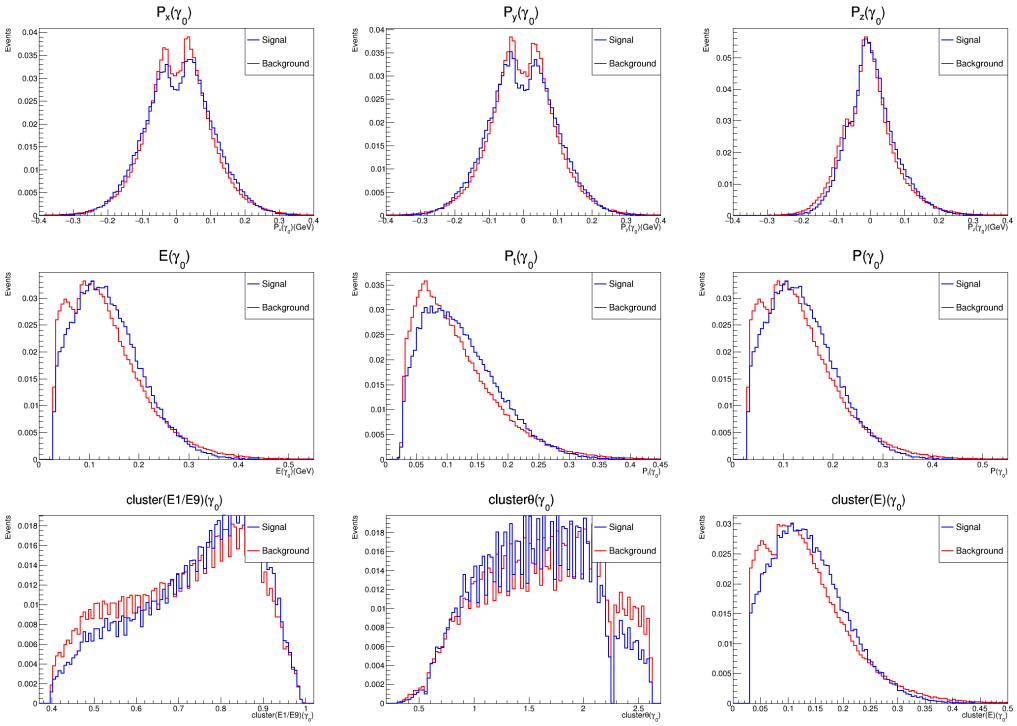

Figure 16: Overlay plots for γ_0 variables

The π^0 meson decays mostly to two photons. They are denoted by γ_0 and γ_1. Figure 16 shows the overlay signal and background distributions for the kinematic variables of γ_0 which includes the distribution of its momentum in x,y and z directions and the energy, transverse momentum and magnitude of momentum. The last row of images correspond to the distributions of $E1/E9$, $clusterθ$ and $clusterE$ which returns the ECL cluster's energy corrected for leakage and background. Figure 17 shows the overlay distributions of the same variables for the γ_1 photon.

All of the overlay distributions in this section are area normalized (the area under both the signal and background distributions are set to unity) which enables us to get a good idea of the amount of distinction which is present between the signal and background. Out of all these variables, some need to be chosen which shows decent amount of discrimination between signal and background which can be used for optimization.

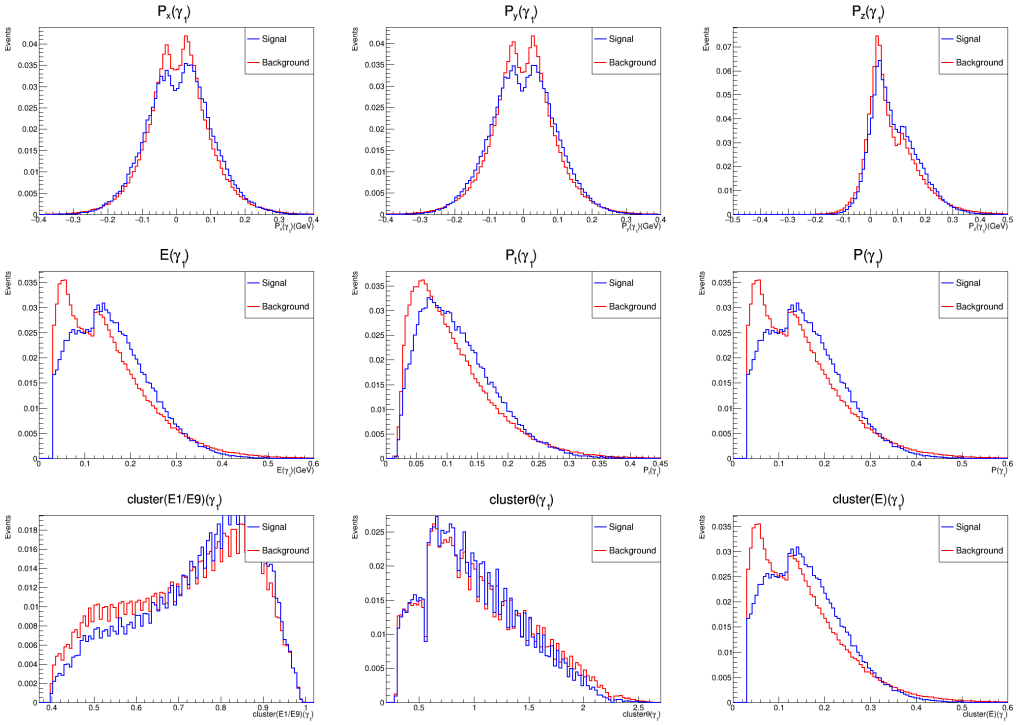

Figure 17: Overlay plots for γ_1 variables

Figure 18 shows some examples of discriminating variables which can be used for optimization. Figures 18(a), 18(b) and 18(c) are the energy, transverse momentum and momentum of the π^+ meson respectively. Figure 18(d) and 18(e) are the momentum and transverse momentum of the π^0 meson.

$p(\pi^+)$ or the momentum (Figure 18(c)) of the π^+ meson is a good variable for optimization. There is a peak in the background from 0.0 GeV/c to about 1.0 GeV/c and the signal is flat throughout. If we can apply a cut around 1.0 GeV/c for this variable, then we can remove decent amount of background by retaining good amount of the signal. The exact value of the cut will be determined by the Figure of merit plot, which would be discussed in the next section. Then for each particle in the decay chain, variables will be investigated and optimized in consecutive rounds of optimization. Particles (for which variables will be chosen) will be selected in a bottom-up approach starting from final state particles of the decay chain. As mentioned above, the first round of optimization will be done using $p(\pi^+)$. In each round of optimization, the signal selection and background rejection percentages will be calculated. The prime variable to tag the decay mode, which is ΔM or the mass difference between D^{*0} and D^0 will be checked after every round of optimization in order to calculate the efficiency which is the ratio of the number of signal events after an optimization to the number of signal events

with pre-selection.

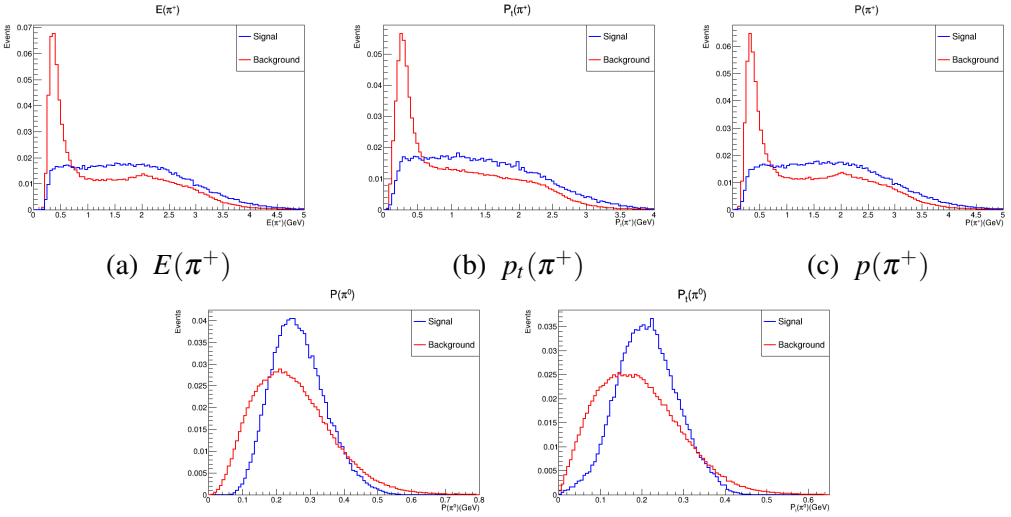

(a) $E(\pi^+)$ (b) $p_t(\pi^+)$ (c) $p(\pi^+)$

(d) $p(\pi^0)$ (e) $p_t(\pi^0)$

Figure 18: Examples of discriminating variables

3.2.2 Optimization of $p(\pi^+)$

Optimization of the momentum of π^+ has been done. A python code was used to incorporate the algorithm that has been stated in the introduction of section 3.2. Signal selection and background rejection efficiencies for each cut value was computed. Finally a cut value for the momentum was chosen so as to reduce background by retaining as much signal as possible.

Figure 19(a) shows the area normalized overlay plots for the signal and background distribution of π^+'s momentum. Figure of merit plot was obtained for this variable and is shown in Figure 19(b).

FOM shows a maxima in a range 0.2 to 0.8 GeV/c. On investigating the computed values of signal selection and background rejection (for every cut value), an optimum value for the cut was selected.

Selected cut value:

$$p(\pi^+) > 0.58\ GeV/c$$

for which the signal selection and background rejection percentages are:

$$\varepsilon_s \times 100\% \approx 89\%\ and\ (1-\varepsilon_b) \times 100\% \approx 35\%$$

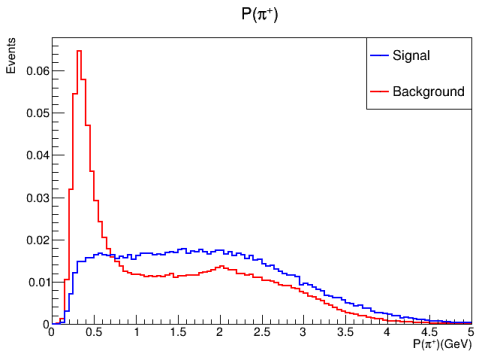

(a) Overlay plot of signal and background for p(π^+)

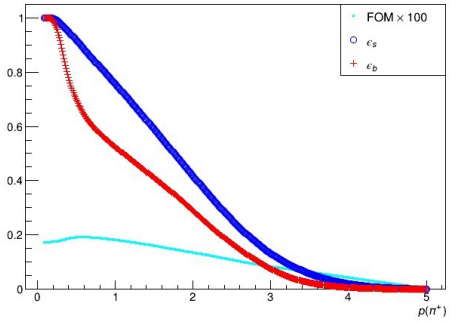

(b) FOM,ε_s and ε_b for p(π^+)

Figure 19

Figure 20 shows a comparison of the mass difference variable before and after the first optimization. Figure 20(a) is the distribution of mass difference before first optimization and Figure 20(b) is the distribution of mass variable after first optimization.

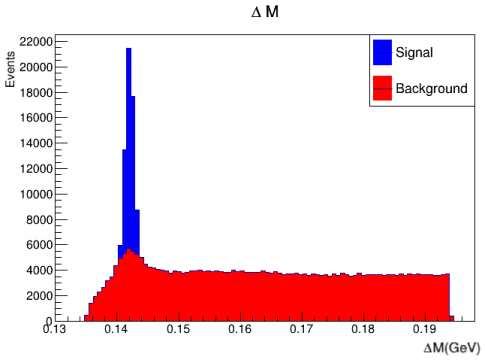

(a) ΔM before 1st optimization

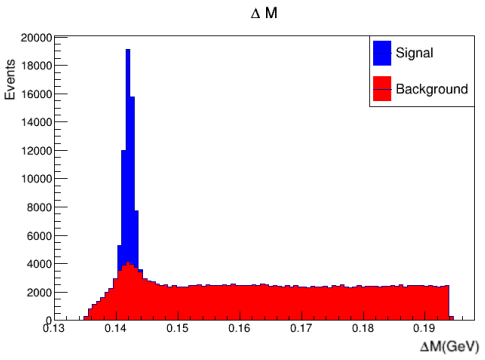

(b) ΔM after 1st optimization

Figure 20

From Figure 20, it is evident that there has been a decrease in the number of events in both signal and background after first optimization. The number of signal events before optimization (with pre-selection only) was 81481 and number of background events was 328674. After first optimization, the numbers are 72565 and 214221 for signal and background respectively. The number of signal events

before and after optimization are required to calculate efficiency as follows:

$$efficiency = \frac{Number\ of\ signal\ events\ after\ optimization}{Number\ of\ signal\ events\ with\ pre-selection} = \frac{72565}{81481} \times 100\% = 89.06\%$$

So the efficiency after first optimization is 89.06%. After optimizing $p(\pi^+)$ which is a variable of the π^+ meson, other variables of other particles in the decay chain needs to be investigated.

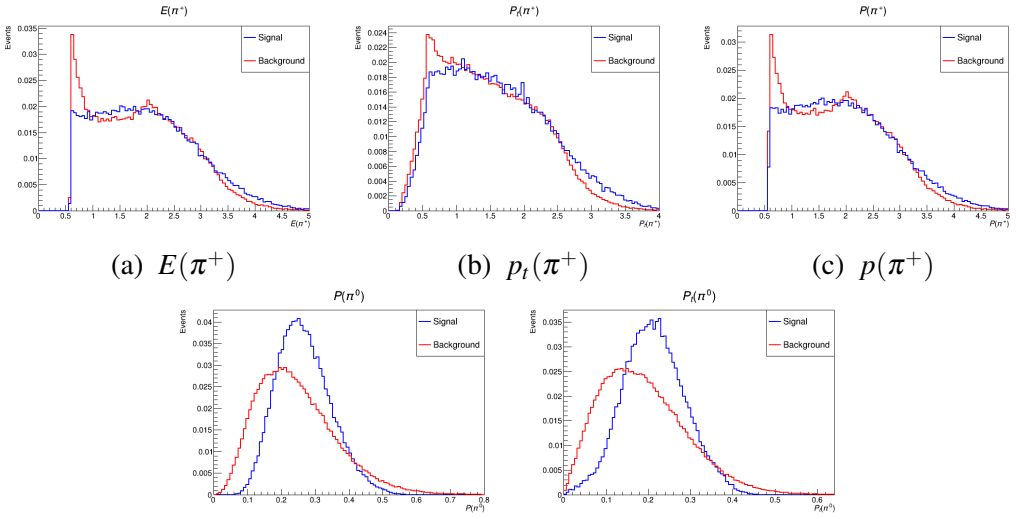

(a) $E(\pi^+)$ (b) $p_t(\pi^+)$ (c) $p(\pi^+)$

(d) $p(\pi^0)$ (e) $p_t(\pi^0)$

Figure 21: Discriminating variables after 1st optimization

On investigating the same variables as in Figure 18, it is observed from Figure 21 that the variables associated to the π^+ meson are no longer discriminating after first optimization. This is because, one of these variables which is the momentum has been optimized which has altered the distributions of the other two variables of π^+ meson as well. However Figure 21(d) and Figure 21(e) are still discriminating.

The second round of optimization, which would incorporate the outcome of the first optimization will be done with $p(\pi^0)$ to further reduce the background. Efficiency after second round of optimization will also be calculated.

3.2.3 Optimization of $p(\pi^0)$

Figure 22(a) shows the area normalized overlay plots for the signal and background distribution of π^0's momentum. Figure of merit plot was obtained for this variable and is shown in Figure 22(b).

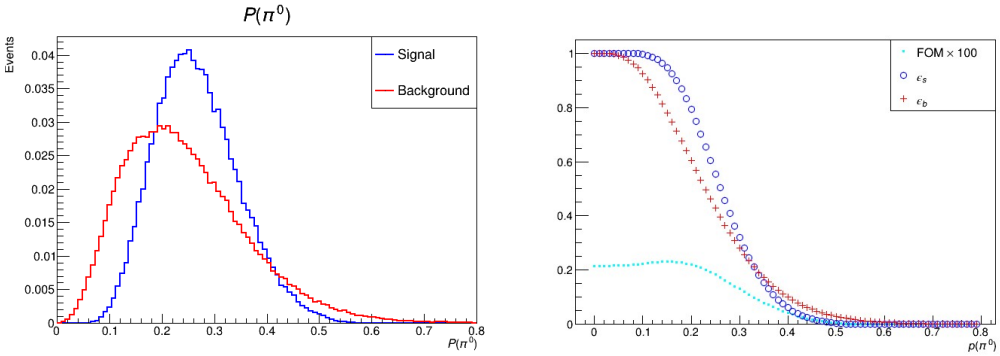

(a) Overlay plot of signal and background for P(π^0)

(b) FOM,ε_s and ε_b for P(π^0)

Figure 22

FOM shows a maxima in a range 0.12 to 0.26 GeV/c. On investigating the computed values of signal selection and background rejection (for every cut value), an optimum value for the cut was selected.

Selected cut value:

$$p(\pi^0) > 0.20\ GeV/c$$

for which the signal selection and background rejection percentages are:

$$\varepsilon_s \times 100\% \approx 79\%\ and\ (1-\varepsilon_b) \times 100\% \approx 40\%$$

Figure 23 shows a comparison of the mass difference variable before and after the second optimization. Figure 23(a) is the distribution of mass difference after first optimization and Figure 23(b) is the distribution of mass variable after second optimization. From Figure 23, it is evident that there has been a decrease in the number of events in both signal and background after second optimization. Number of signal and background events after second optimization are 57495 and 129470 respectively.

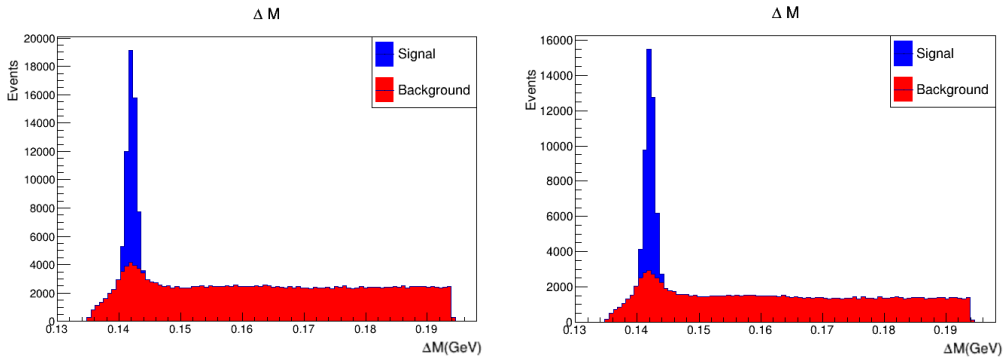

(a) ΔM after 1st optimization (b) ΔM after 2nd optimization

Figure 23

The efficiency after second optimization (having the outcome of first optimization incorporated) is:

$$efficiency = \frac{Number\ of\ signal\ events\ after\ optimization}{Number\ of\ signal\ events\ with\ pre-selection} = \frac{57495}{81481} \times 100\% = 70.56\%$$

So the efficiency after second optimization is 70.56%. After optimizing $p(\pi^+)$ and $p(\pi^0)$, the outcome of the variables in Figure 21 is shown in Figure 24.

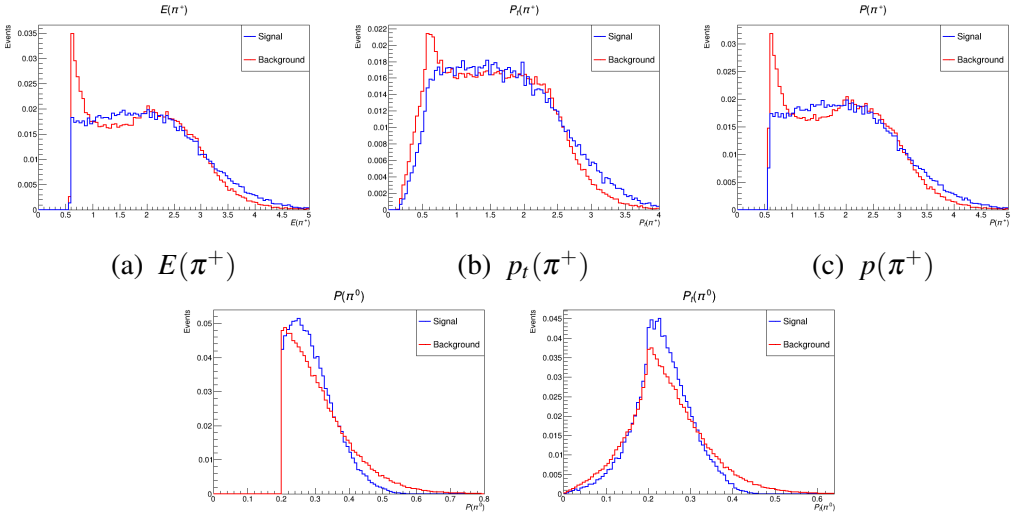

(a) $E(\pi^+)$ (b) $p_t(\pi^+)$ (c) $p(\pi^+)$

(d) $p(\pi^0)$ (e) $p_t(\pi^0)$

Figure 24: previously discriminating variables after second optimization

From Figure 24 it is evident that none of the π^+ and π^0 variables are discriminating after second optimization. Hence variables of other particles needs to be investigated.

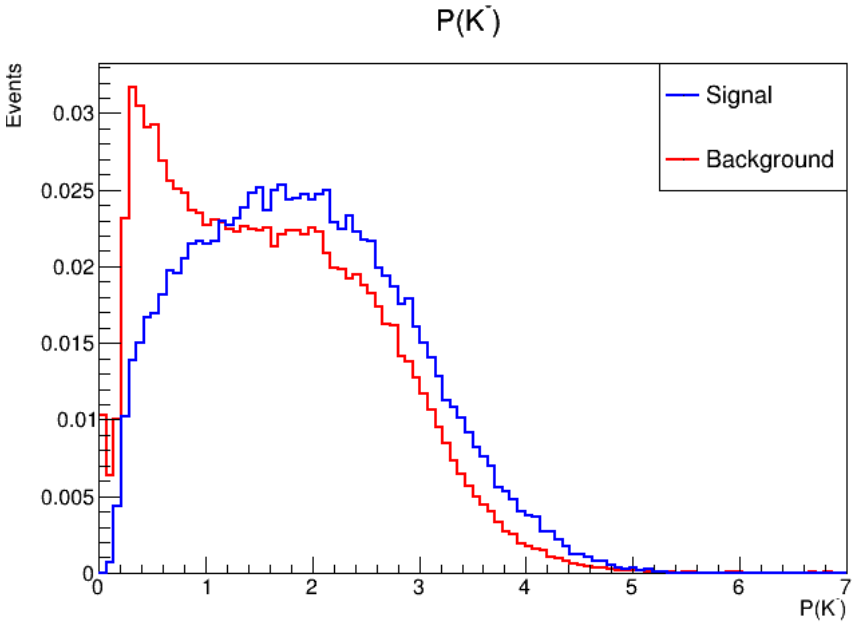

Figure 25: $p(K^-)$

Figure 25 shows the distribution of the momentum of K^- which shows discrimination after second optimization. There is a peaking in the background in the range 0.0 GeV/c to 1.2 GeV/c which if removed using a suitable cut value will decrease the overall background present to some extent.

The third round of optimization, which would incorporate the outcome of the first and second optimization will be done with $p(K^-)$ to further reduce the background. Efficiency after third round of optimization will also be calculated.

3.2.4 Optimization of $p(K^-)$

Figure 26(a) shows the area normalized overlay plots for the signal and background distribution of K^-'s momentum. Figure of merit plot was obtained for this variable and is shown in Figure 26(b).

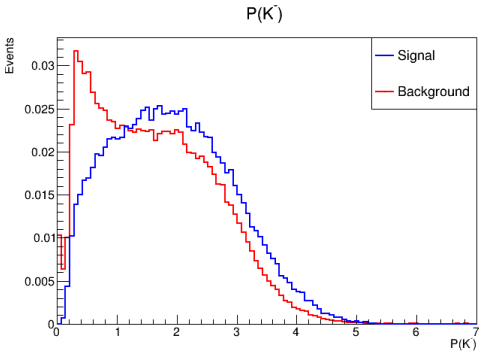

(a) Overlay plot of signal and background for p(K^-)

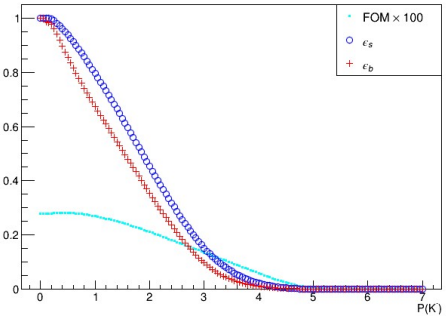

(b) FOM,ε_s and ε_b for P(K^-)

Figure 26

FOM in Figure 26(b) is almost flat in the range 0.0 to 1.4 GeV/c, thereafter it decreases. On investigating the computed values of signal selection and background rejection (for every cut value), an optimum value for the cut was selected.

Selected cut value:

$$p(K^-) > 1.2\ GeV/c$$

for which the signal selection and background rejection percentages are:

$$\varepsilon_s \times 100\% \approx 79\%\ and\ (1-\varepsilon_b) \times 100\% \approx 39\%$$

Figure 27 shows a comparison of the mass difference variable before and after the third optimization. Figure 23(a) is the distribution of mass difference after second optimization and Figure 23(b) is the distribution of mass variable after third optimization. From Figure 27, it is evident that there has been a decrease in the number of events in both signal and background after third optimization. Number of signal and background events after third optimization are 42052 and 78787 respectively.The efficiency after third optimization (having the outcome of first and second optimization incorporated) is:

$$efficiency = \frac{Number\ of\ signal\ events\ after\ optimization}{Number\ of\ signal\ events\ with\ pre-selection} = \frac{42052}{81481} \times 100\% = 51.61\%$$

Figure 28 shows the effect of 3rd optimization on the momentum of K^-.

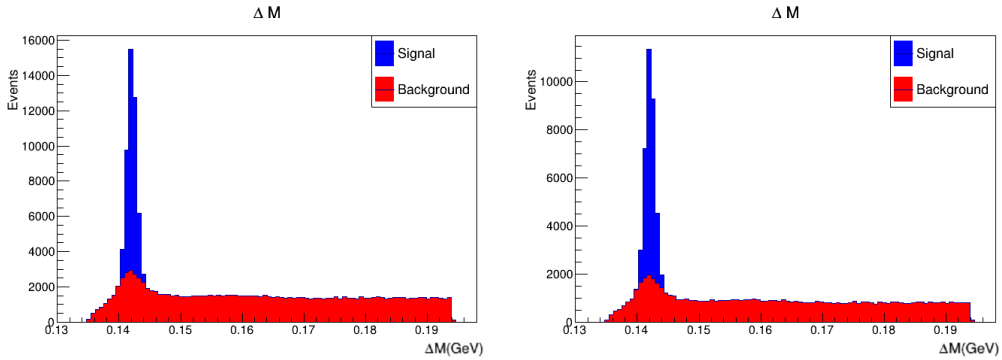

(a) ΔM after 2nd optimization (b) ΔM after 3rd optimization

Figure 27

From Figure 28, it is evident that there is no proper discrimination any more in $p(K^-)$. The peak in the background which was present has been removed after optimization.

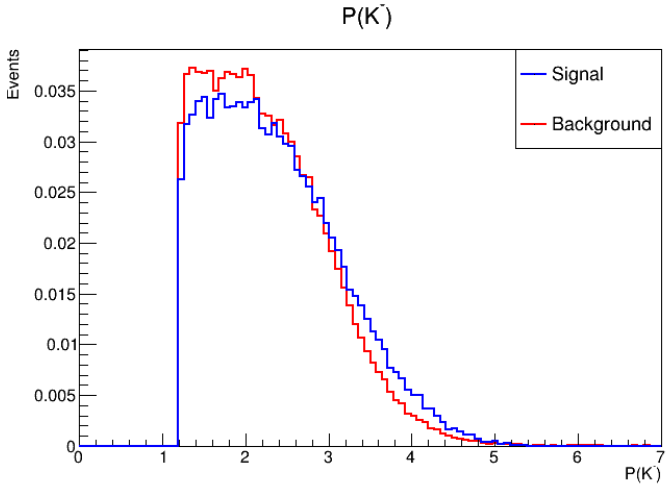

Figure 28: $P(K^-)$

Among final state particles, only γ variables have not been optimized yet. Since there is a pre-selection on the energy of the two photons (γ_0 and γ_1), energy of the photons can be chosen for optimization. Figure 29(a) and Figure 29(b) shows the energy distributions of the photons present in the decay chain after third optimization. These are not discriminating enough, hence we expect to get a very loose cut for them.

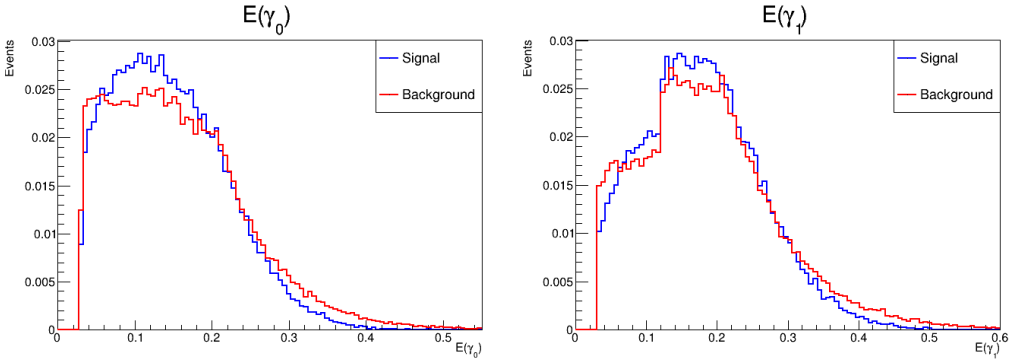

(a) $E(\gamma_0)$ (b) $E(\gamma_1)$

Figure 29

In the next two optimization rounds, these two γ variables shown in Figure 29 would be optimized to obtain loose cuts on them to reduce some background without the loss of much signal.

3.2.5 Optimization of $E(\gamma_0)$

Figure 30(a) shows the area normalized overlay plots for the signal and background distribution of γ_0's energy. Figure of merit plot was obtained for this variable and is shown in figure 30(b).

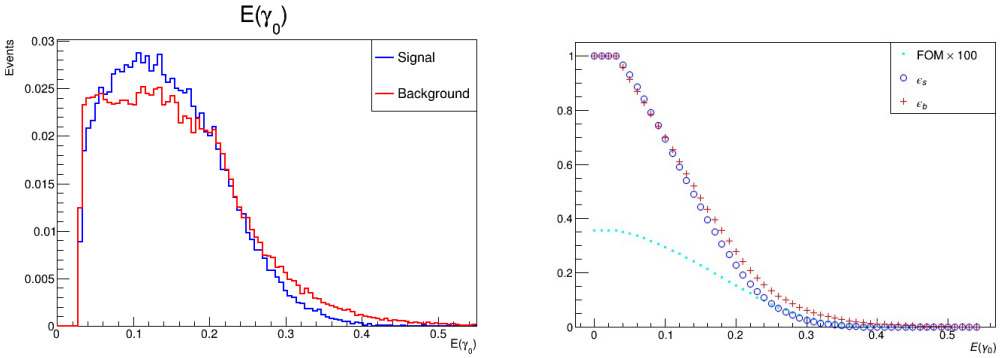

(a) Overlay plot of signal and background for E(γ_0)

(b) FOM,ε_s and ε_b for E(γ_0)

Figure 30

Since this variable is not discriminating enough, the FOM does not give much insight as to which cut value should be chosen. However from the overlay distribution in Figure 30(a), it can be seen that if a cut is made at a range from 0.04 GeV/c^2 to 0.08 GeV/c^2, a small amount of background can be removed with minimum reduction of the signal. Further, on investigating the computed values of signal selection and background rejection (for every cut value), an optimum value for the cut was selected.

Selected cut value:

$$E(\gamma_0) > 0.06\ GeV/c^2$$

for which the signal selection and background rejection percentages are:

$$\varepsilon_s \times 100\% \approx 88\%\ and\ (1-\varepsilon_b) \times 100\% \approx 13\%$$

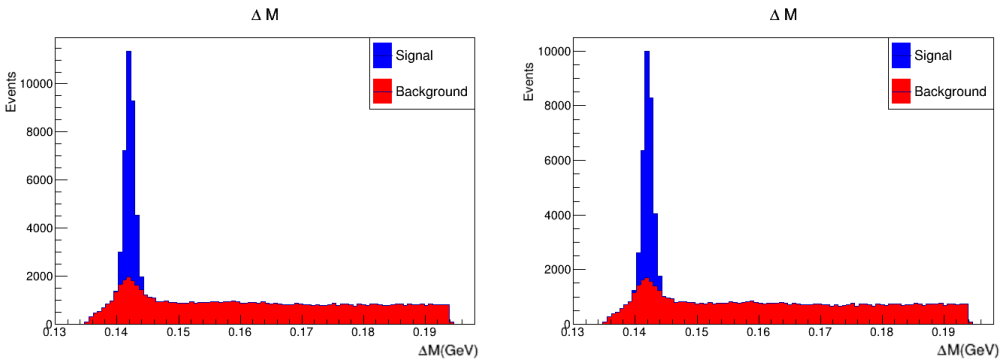

(a) ΔM after 3rd optimization (b) ΔM after 4th optimization

Figure 31

Figure 31 shows a comparison of the mass difference variable before and after the fourth optimization. Figure 31(a) is the distribution of mass difference after third optimization and Figure 31(b) is the distribution of mass variable after fourth optimization. From Figure 31, it is evident that there has been a little decrease in the number of events in both signal and background after fourth optimization. Number of signal and background events after fourth optimization are 37183 and 68529 respectively. The efficiency after fourth optimization (having the outcome of first, second and third optimization incorporated) is:

$$efficiency = \frac{Number\ of\ signal\ events\ after\ optimization}{Number\ of\ signal\ events\ with\ pre-selection} = \frac{37183}{81481} \times 100\% = 45.63\%$$

Figure 32(a) and figure 32(b) shows the energy distributions of the photons (γ_0 and γ_1 respectively) present after fourth optimization. From Figure 32(a), it can be concluded that if further optimization of this variable is done, it would lead to a considerable loss of signal along with the background. A loose cut can still be applied on the energy of γ_1 as seen from Figure 32(b) to reduce a small amount of background without reducing the signal much.

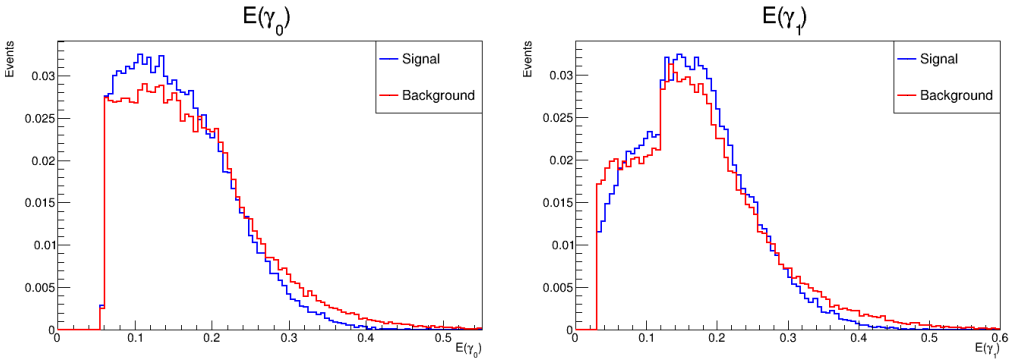

(a) $E(\gamma_0)$ (b) $E(\gamma_1)$

Figure 32

In the next round of optimization, $E(\gamma_1)$ will be optimized to obtain a loose cut on this variable.

3.2.6 Optimization of $E(\gamma_1)$

Figure 33(a) shows the area normalized overlay plots for the signal and background distribution of γ_1's energy. Figure of merit plot was obtained for this variable and is shown in Figure 33(b).

Similarly as for $E(\gamma_0)$ this variable is also not discriminating enough, and hence the FOM does not give much insight as to which cut value should be chosen. However from the overlay distribution in Figure 33(a), it can be seen that if a cut is made at a range from 0.02 GeV/c^2 to 0.08 GeV/c^2, a small amount of background can be removed with minimum reduction of the signal. Further, on investigating the computed values of signal selection and background rejection (for every cut value), an optimum value for the cut was selected.

Selected cut value:

$$E(\gamma_1) > 0.06\ GeV/c^2$$

for which the signal selection and background rejection percentages are:

$$\varepsilon_s \times 100\% \approx 93\%\ and\ (1-\varepsilon_b) \times 100\% \approx 10\%$$

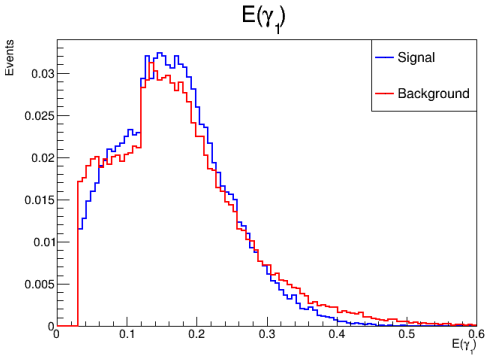

(a) Overlay plot of signal and background for E(γ_1)

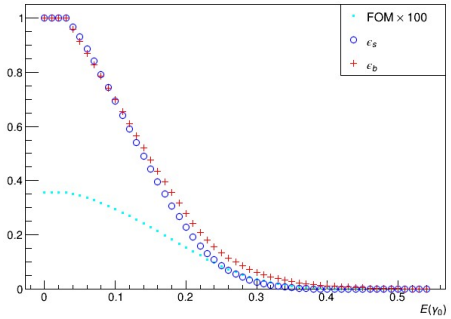

(b) FOM,ε_s and ε_b for E(γ_1)

Figure 33

Figure 34 shows a comparison of the mass difference variable before and after the fifth optimization. Figure 33(a) is the distribution of mass difference after fourth optimization and Figure 33(b) is the distribution of mass variable after fifth optimization.

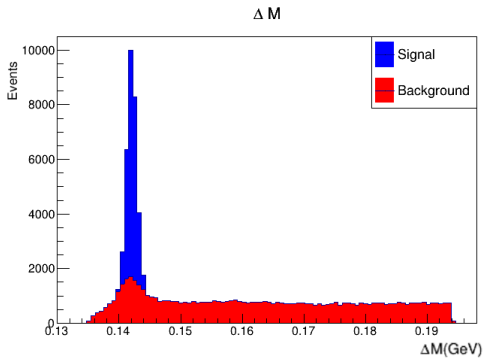

(a) ΔM after 4th optimization

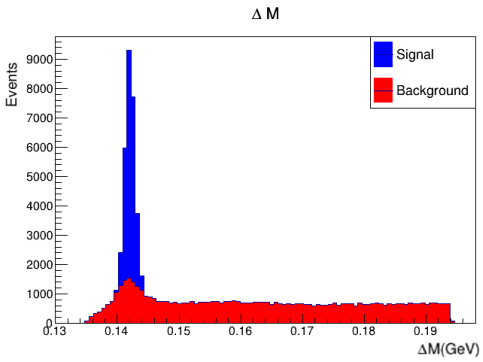

(b) ΔM after 5th optimization

Figure 34

From Figure 34, it is evident that there has been a little decrease in the number of events in both signal and background after fifth optimization. Number of signal and background events after fifth optimization are 34508 and 62126 respectively.

The efficiency after fifth optimization (having the outcome of first, second, third and fourth optimization incorporated) is:

$$efficiency = \frac{Number\ of\ signal\ events\ after\ optimization}{Number\ of\ signal\ events\ with\ pre-selection} = \frac{34508}{81481} \times 100\% = 42.35\%$$

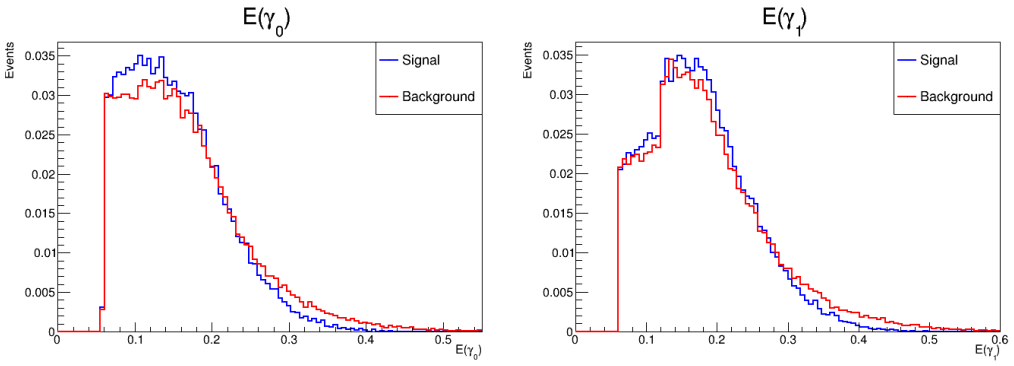

(a) $E(\gamma_0)$ (b) $E(\gamma_1)$

Figure 35

Figure 35(a) and Figure 35(b) shows the energy distributions of the photons (γ_0 and γ_1 respectively) present after fifth optimization. From both Figure 35(a) and Figure 35(b), it can be concluded that if further optimization of these variables are done, it would lead to a considerable loss of signal along with the background.

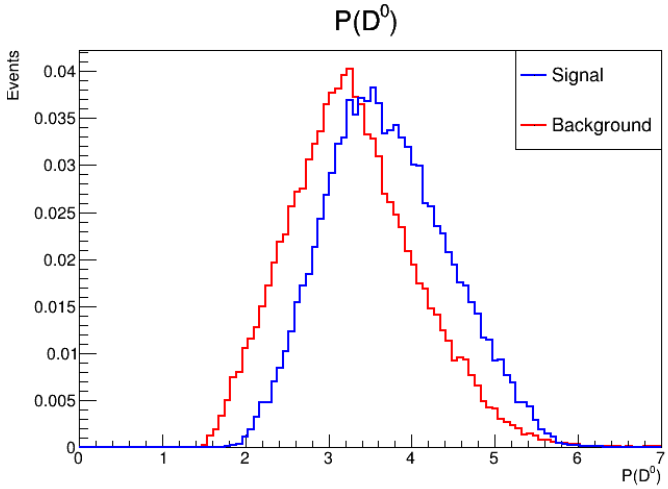

Figure 36: $p(D^0)$

In order to reduce the background further, variables associated to a final state particle like the D^0 meson must me investigated and there are no variables related to the final state particles which can be optimized.

Figure 36 shows the area normalized overlay distribution of the momentum of the D^0 meson. This variable shows good amount of discrimination between signal and background. This variable would be used for optimization in the next round of optimization to reduce background.

3.2.7 Optimization of $p(D^0)$

Figure 37(a) shows the area normalized overlay plots for the signal and background distribution of D^0's momentum. Figure of merit plot was obtained for this variable and is shown in Figure 37(b).

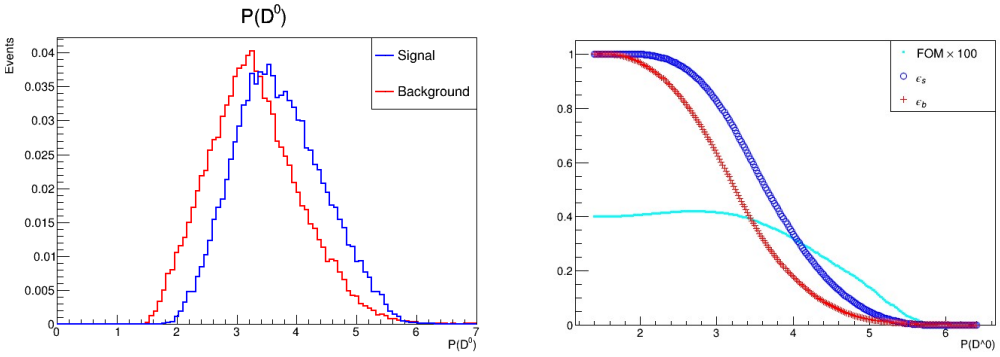

(a) Overlay plot of signal and background for p(D^0)

(b) FOM,ε_s and ε_b for p(D^0)

Figure 37

FOM shows a maxima in a range 2.4 to 3.4 GeV/c. On investigating the computed values of signal selection and background rejection (for every cut value), an optimum value for the cut was selected.

Selected cut value:

$$p(D^0) > 3.00\ GeV/c$$

for which the signal selection and background rejection percentages are:

$$\varepsilon_s \times 100\% \approx 83\%\ and\ (1-\varepsilon_b) \times 100\% \approx 37\%$$

Figure 38 shows a comparison of the mass difference variable before and after the sixth optimization. Figure 38(a) is the distribution of mass difference after fifth optimization and figure 38(b) is the distribution of mass variable after sixth optimization. From figure 38, it is evident that there has been a decrease in the number of events in both signal and background after sixth optimization. Number of signal and background events after sixth optimization are 28534 and 39417 respectively.

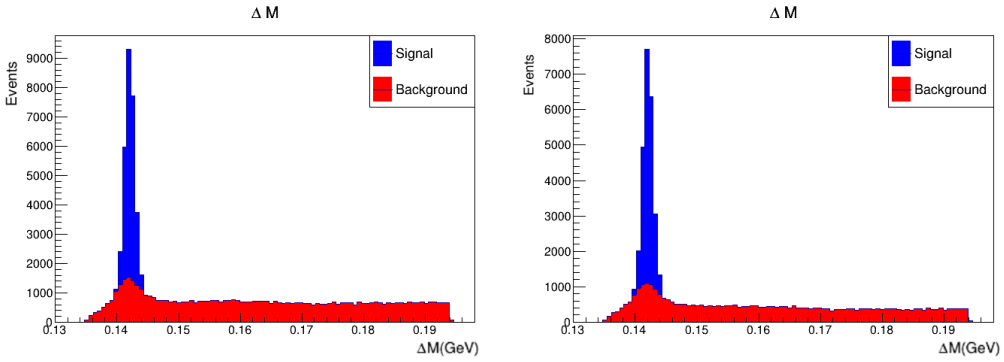

(a) ΔM after 5th optimization (b) ΔM after 6th optimization

Figure 38

The efficiency after sixth optimization (having the outcome of first, second, third, fourth and fifth optimization incorporated) is:

$$efficiency = \frac{Number\ of\ signal\ events\ after\ optimization}{Number\ of\ signal\ events\ with\ pre-selection} = \frac{28534}{81481} \times 100\% = 35.02\%$$

Calculation of total background rejection efficiency after sixth optimization:

$$Total\ number\ of\ background\ events\ with\ pre-selection\ =\ 328674$$

$$Total\ number\ of\ background\ events\ after\ 6th\ optimization\ =\ 39417$$

$$background\ rejection\ efficiency = 1 - \frac{Number\ of\ background\ events\ after\ 6th\ optimization}{Number\ of\ background\ events\ with\ pre-selection}$$

$$= (1 - \frac{39417}{328674}) \times 100\% = 88.01\%$$

Figure 39 shows a comparison of the mass distributions of D^0 and D^{*0} and their mass difference with pre-selection (Figure 39(a),Figure 39(b) and Figure 39(c) respectively) and after 6th optimization ((Figure 39(d),Figure 39(e) and Figure 39(f) respectively)). There has been considerable amount of background rejected (about 90% as evident from the background rejection efficiency). However the signal has also been brought down to about 35%. Further optimization would decrease the signal more which would make the distribution difficult for fitting to calculate the yield. Hence, no further optimization will be done.

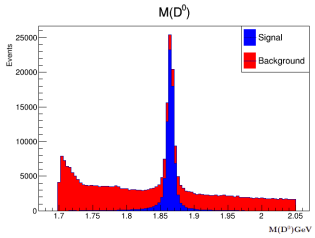

(a) $M(D^0)$ with pre-selection

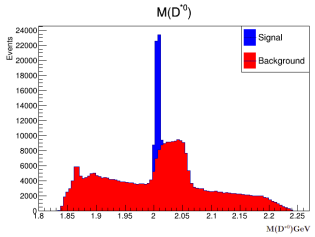

(b) $M(D^{*0})$ with pre-selection

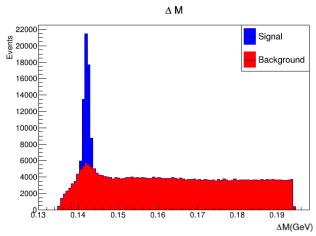

(c) ΔM with pre-selection

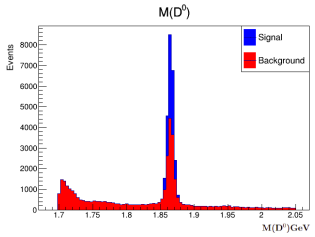

(d) $M(D^0)$ after 6th optimization

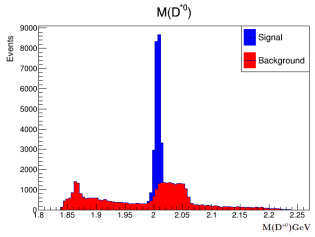

(e) $M(D^{*0})$ after 6th optimization

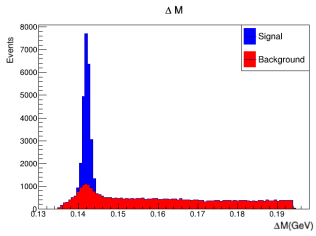

(f) ΔM after 6th optimization

Figure 39: Comparison of mass and mass difference variables before and after optimization

From Figure 39(f), it is observed that the peaking background is still present. It is of interest to investigate the decay modes which constitute this peaking background around the signal region. Recently, in a new release of Basf2, a tool called 'Gen MC Tag' has been incorporated which allows users to to investigate the decay modes which actually contribute in a distribution of a variable which had been reconstructed for a particular decay mode. This tool will be used to investigate decay modes contribute to this peaking background in the mass difference variable present in a range from $0.138 GeV/c^2$ to $0.148 GeV/c^2$.

3.3 Peaking background study

Identifying possible sources of background is important for any analysis in high energy physics. Generic MC samples are used to estimate this background. Here in this analysis, generic MC samples (of $100 fb^{-1}$) have been used which allows for the study of the possible sources of background present.

To guess or identify the possible background one needs to gain or have some experience. In order to identify the background decays, one can look at the mother, grand mother IDs of the reconstructed MC particles. But, tagging with reconstructed level information may fail for partially misreconstructed decays where a fraction of background particles are wrongly reconstructed as signal events. In the Basf2 framework, the isSignal module is present, but it cannot effectively distinguish between signal and background in such cases. Therefore a particle decay needs to be tagged using the generator level information. If it is known that the event is coming from a particular decay chain, the background can easily be understood and tagged.

In the new and latest release of Basf2 (release-06-00-03) a tool has been added which can be used easily and effectively to tag particle decays using generator level information. This tool is called the **GenMCTagTool**[17]. This tool offers registered variables for several final state particles like B^+, B^0, D^+, D^0, D_s^+, etc. The user just needs to add this variable of the the final state particle whose decay is being studied to the ntuple during reconstruction. The variable will take a range of values, each of which corresponds to a particular decay of that final state particle. Thus each entry (which is a set of values for all variables that were saved in the ntuple) corresponds to a particular decay mode as tagged by this registered GenMCTag variable. Using this variable, one can easily select the entries which correspond to a particular decay mode of the final state particle. A plot of the distribution of this decay mode keeping isSignal variable as zero would suggest what kind of contribution (peaking or combinatorial) it has to the total background.

The background present in this analysis is due to the various decay modes present for the D^0 meson. In order to do a background study for this mode, the registered variable in the GenMCTagTool corresponding to all possible decays of D^0 meson needs to be saved in the final ntuple, as discussed before. The name of the registered variable is 'D0Mode' and it returns 136 values corresponding to 136 decays of the D^0 meson. The values range from 1001 to 1136, out of which the value 1017 corresponds to the signal mode of this analysis which is $D^0 \to K^-\pi^+$. All of these 136 decay modes has been investigated to have an idea of the modes which lead to the formation of the peak present in the background of Figure 38(b). The mass difference variable (ΔM) was checked for the background of each of the 135 modes other than the signal mode.

Figure 40 shows the mass difference distribution for the signal mode ($D^0 \to K^-\pi^+$). There is a clear peak near the expected value of the mass difference ($\approx 0.142 GeV/c^2$)[3] and the mean of the distribution ($0.1421 GeV/c^2$) is in good agreement with the expected value. Hence the reconstruction of the signal mode was successful from generic MC samples as input.

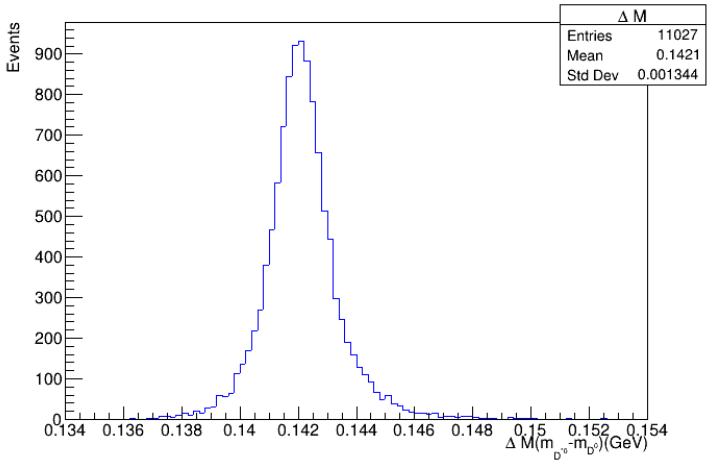

Figure 40: $D^0 \to K^-\pi^+$

For understanding the background, all the rest 135 decay modes of D^0 meson were investigated. Some of the modes had a flat distribution around the signal region ($0.138 GeV/c^2$ to $0.148 GeV/c^2$) and hence it is concluded that they are contributing to the combinatorial background. Figure 40 shows three examples of such decay modes.

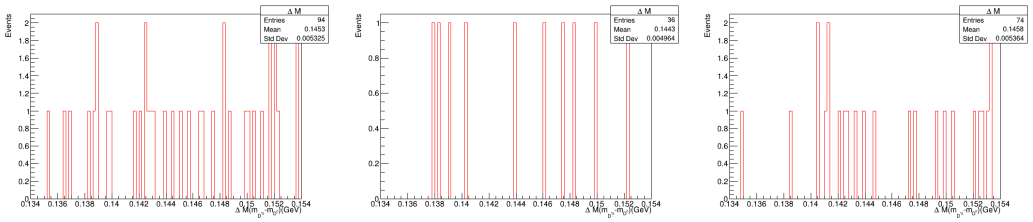

(a) $D^0 \to \pi^-\pi^+\pi^0\pi^0$ (b) $D^0 \to K^0_L K^-\pi^+$ (c) $D^0 \to K^0_L \eta\pi^0$

Figure 41: Examples of decay modes contributing to the combinatorial background

The peaking background is of interest. After investigating the background distributions of all decay modes of the D^0 meson, eight decay modes have been

found to show a peaking distribution around the signal area. The distribution of these eight modes are shown in figure 42.

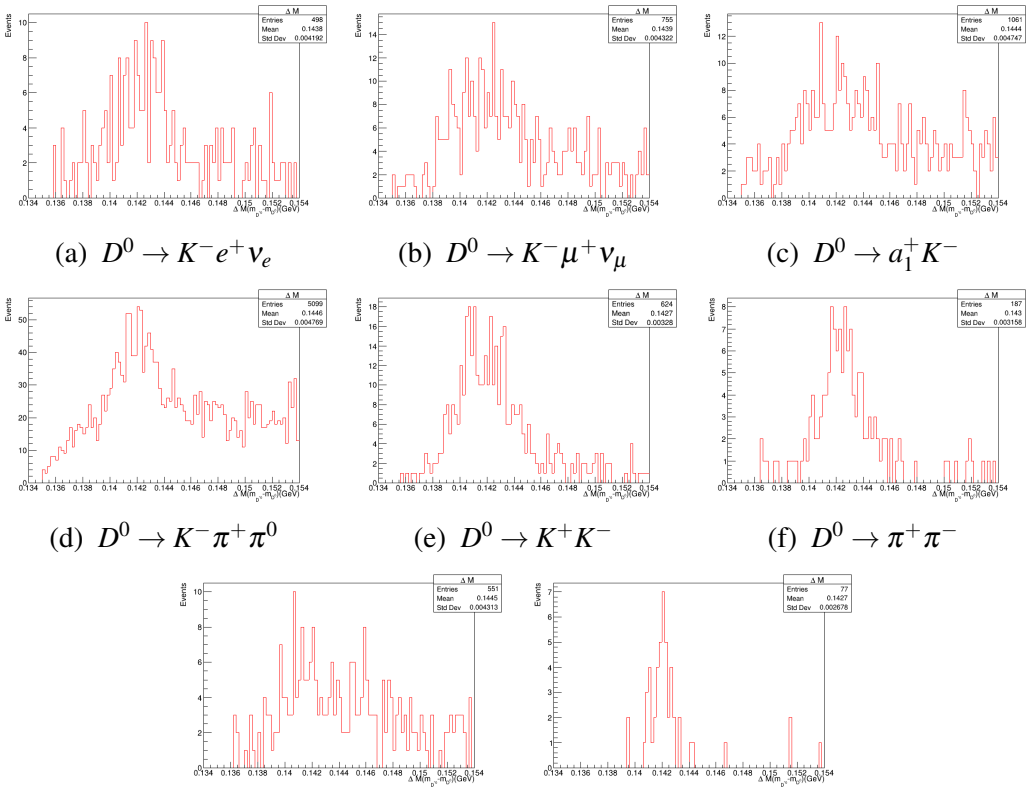

(a) $D^0 \to K^- e^+ \nu_e$ (b) $D^0 \to K^- \mu^+ \nu_\mu$ (c) $D^0 \to a_1^+ K^-$

(d) $D^0 \to K^- \pi^+ \pi^0$ (e) $D^0 \to K^+ K^-$ (f) $D^0 \to \pi^+ \pi^-$

(g) $D^0 \to \pi^+ \pi^- \pi^0$ (h) $D^0 \to \pi^- K^+$

Figure 42: Decay modes contributing to the peaking background

These eight decay modes contribute to the peaking background present in the mass difference distribution present of Figure 38(b) around the signal region ($0.138 GeV/c^2$ to $0.148 GeV/c^2$).

3.4 Fitting

After reducing the background through optimization, we now fit the prime variable of the analysis (ΔM here) with a suitable probability density function to calculate accurately the mean and the yield of signal and background from the total data set. There are certain parameters which determines the quality of a fit. Here, the χ^2/ndf (ndf = number of degrees of freedom) and the 'pull' distributions are checked to determine the quality of the fit. If the chosen probability density function fits the data properly, then the χ^2/ndf value is close to one and the pull distribution (which gives a distribution of the deviation of the probability density function with the data) is within ± 3 throughout the entire range of the data.

For fitting, a pre-loaded package in ROOT called Roofit has been used. The basic procedure of doing any fit using roofit is to first load the Roofit package in a Root macro. Then one needs to load the events from the ntuple constaining the variable to be investigated, to a memeber function of Roofit known as 'RooDataSet'. This creates an unbinned data set for the variable which can then be used for fitting. Then after, the pdf of the probability density function needs to be guessed and defined. Then one needs to fit the data and plot the outcome.

Here, first the signal will be investigated and fitted with a suitable probability density function. Then the same will be done for the background. Ideally, if a peaking background is present along with a combinatorial part, it is better to deal with them separately. In this analysis, both the background components has been dealt with together in a single fit and the parameters for the same has been noted. Then finally the data sets of signal and background along with the probability density functions used to fit them individually were added to obtain a fit of the total data set. The expected mean from this total fit should be close to the expected value of the mass difference ($0.142014 \pm 0.000030\ GeV/c^2$)[3]. The yield of signal and background would be obtained from this fitting of the total data set.

3.4.1 Probability density functions

In this section, some of the probability density functions (pdf) which were used in the analysis will be discussed in brief. In order to tune the parameters of a probability density function properly to obatain a good fit to a certain data set, it is important to know the effect of changing a certain parameter of a certain pdf. Here, the main focus would be to understand the effect of changing each parameters of the pdfs that were used for fitting in this analysis.

1. Gaussian pdf: The Gaussian pdf is the most commonly used probability density function used to fit any kind of peak in a distribution. The probability density function has been stated in equation 1. The Gaussian probability density function

is characterised by two parameters, the mean (μ) and the standard deviation (σ).

$$f(x;\mu,\sigma) = \frac{1}{\sigma\sqrt{2\pi}} e^{-\frac{(x-\mu)^2}{2\sigma^2}} \tag{1}$$

Figure 43(a) and Figure 43(b) shows the effect of varying the parameters μ and σ respectively. These plots have been generated using Roofit.

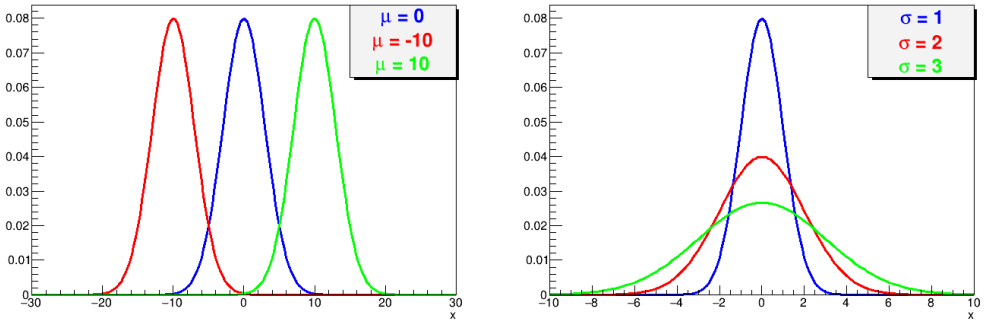

(a) variation of μ with $\sigma = 3$ (b) variation of σ with $\mu = 0$

Figure 43: Normalized Gaussian distribution

In Figure 43(a), the mean (μ) was varied keeping the standard deviation (σ) fixed at $\sigma = 3$. The red, blue and green curves have means $\mu = -10$, $\mu = 0$ and $\mu = 10$ respectively. Thus it is clear that the parameter μ controls the position of the peak in a Gaussian distribution. In Figure 43(b), the standard deviation (σ) was varied keeping the mean (μ) fixed at $\mu = 0$. The blue, red and green curves have standard deviations $\sigma = 1$, $\sigma = 2$ and $\sigma = 3$ respectively. Thus, the parameter σ, controls the width of the peak of a Gaussian distribution. In Roofit, the gaussian distribution is incorporated using the 'RooGaussian' module.

2. Crystal Ball pdf: The Crystal Ball probability density function has been stated in equation 2. The expression is quite complicated but, effectively it behaves like a special kind of a Gaussian distribution characterised by an extended tail on one of its sides.

$$f(x;\alpha,n,\mu,\sigma) = N \cdot \left\{ \begin{array}{ll} e^{-\frac{(x-\mu)^2}{2\sigma^2}}, & \text{if } \frac{x-\mu}{\sigma} > -\alpha \\ A \cdot (B - \frac{x-\mu}{\sigma})^{-n}, & \text{if } \frac{x-\mu}{\sigma} \leq -\alpha \end{array} \right\} \tag{2}$$

where $A = \left(\frac{n}{|\alpha|}\right)^n \cdot e^{-\frac{|\alpha|^2}{2}}$, $B = \frac{n}{|\alpha|} - |\alpha|$, $C = \frac{n}{|\alpha|} \cdot \frac{1}{n-1} \cdot e^{-\frac{|\alpha|^2}{2}}$, $D = \sqrt{\frac{\pi}{2}} \left(1 + erf\left(\frac{|\alpha|}{\sqrt{2}}\right)\right)$, $N = \frac{1}{\sigma(C+D)}$

Apart from the usual mean (μ) and standard deviation (σ) parameters of regular Gaussian distribution, the Crystal ball distribution has two more parameters which are 'α' and 'n'. The parameters μ and σ has similar effect on the Crystal ball distribution as they had on the Gaussian distribution. Figure 44(a) and Figure 44(b) shows the effect of varying the parameter α. Figure 44(c) shows the effect of varying the parameter n. These plots have been generated using Roofit.

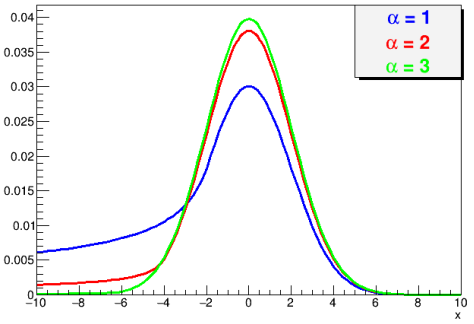

(a) variation of $+\alpha$ with $\mu = 0$, $\sigma = 2$, $n = 0.5$

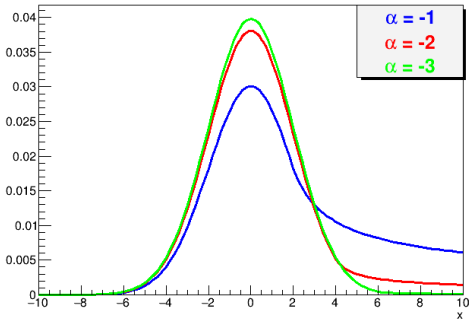

(b) variation of $-\alpha$ with $\mu = 0$, $\sigma = 2$, $n = 0.5$

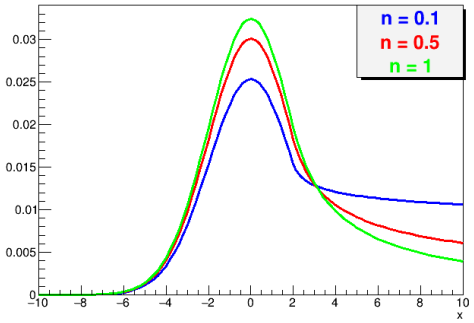

(c) variation of n with $\mu = 0$, $\sigma = 2$, $\alpha = -1$

Figure 44: Normalized Crystal Ball distribution

Although α and n affect the entire Crystal Ball distribution as a whole, primarily they both determine the extension that is present in the Crystal Ball probability density function. In Figure 44(a), the parameter α was varied using positive values, keeping all the other parameters fixed at $\mu = 0$, $\sigma = 2$ and $n = 0.5$. In Figure 44(b) also the parameter α was varied, but now using negative values, keeping all the other parameters fixed as in the previous case. From these two figures it is evident that depending on whether the value of the parameter α is positive or negative, the extended tail of the Crystal Ball distribution would be on the left or right side respectively. The magnitude of the parameter α determines the level of

extension this tail would have. In Figure 44(a) the blue, red and green curves have $\alpha = 1$, $\alpha = 2$ and $\alpha = 3$ respectively. Similarly in Figure 44(b) the blue, red and green curves have $\alpha = -1$, $\alpha = -2$ and $\alpha = -3$ respectively. It is observed that, as the magnitude of α increases, the extended tail of the Crystal Ball distribution lowers. As the magnitude of α decreases, the extended tail of the Crystal Ball distribution is raised.

In Figure 44(c), the parameter n was varied keeping all other parameters fixed at $\mu = 0$, $\sigma = 2$ and $\alpha = -1$. The blue, red and green curves have $n = 0.1$, 0.5 and 1 respectively. It is observed that this parameter controls the origin of the extended tail in a Crystal Ball distribution. A lower value of n leads to a sharp transition at the origin of this extension. If the value of n is high, the transition is smooth which also lowers the extension to a certain extent. In Roofit, the Crystal Ball distribution is incorporated using the 'RooCBShape' module.

3. Threshold pdf: The Gaussian and Crystal Ball probability density functions are common distributions which are used normally for fitting various data sets. Thus, these distributions are built-in or pre-defined in Roofit. However, sometimes in an analysis, one needs to specially define a probability density function so as to fit a certain data set. This is done using the 'RooGenericPdf' module of Roofit. This module allows the users to define any probability density function which is not pre-defined in Roofit. A Threshold function has been defined and used in this analysis, whose definition has been given in equation 3. In literature, this probability density function has been used in many analysis for fitting the combinatorial background in the mass difference (ΔM) of heavy mesons (D^{*0} and D^0 in this analysis).

$$f(x;t_h,a,b) = \left\{ \begin{array}{ll} (x-t_h)^2 e^{\left[a(x-t_h)+b(x-t_h)^2\right]}, & \text{if } x \geq t_h \\ 0, & \text{if } x < t_h \end{array} \right\} \tag{3}$$

This Threshold probability density function is characterised by three parameters which are t_h, a and b. Figure 45(a), Figure 45(b) and Figure 45(c) shows the effect of varying t_h, a and b respectively. These plots have also been generated using Roofit. The range of the x-axis in these figures has been chosen similar to that present for the range of the mass difference (ΔM).

All the three parameters of the threshold probability density function affect the distribution as a whole. However each parameter parameter primarily affects a certain region of the distribution. In Figure 45(a), the parameter t_h has been varied and the other two parameters have been kept constant at $a = -130$ and $b = 1000$. The blue,red and green curves correspond to $t_h = 0.130$, $t_h = 0.140$ and $t_h = 0.150$. From this figure it is evident that primarily, the parameter t_h determines from where on the x-axis the distribution would start. The distribution starts at the

value of the parameter t_h. It also affects the initial height of the distribution which increases with increasing t_h.

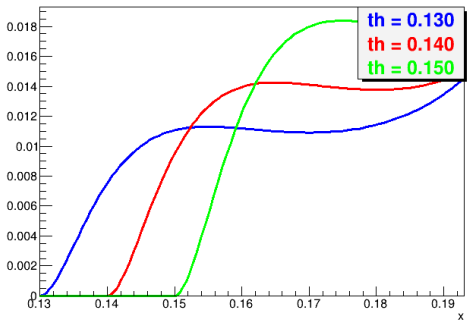

(a) variation of t_h with $a = -130$, $b = 1000$

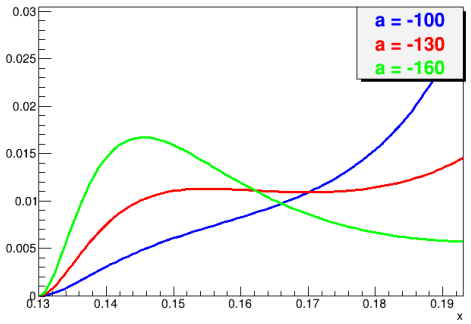

(b) variation of a with $t_h = 0.130$, $b = 1000$

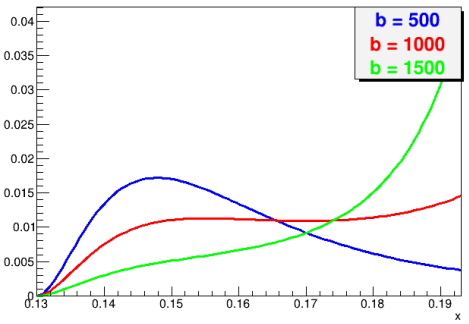

(c) variation of b with $t_h = 0.130$, $a = -130$

Figure 45: Normalized Threshold distribution

In Figure 45(b), the parameter a has been varied and the other two parameters have been kept constant at $t_h = 0.130$ and $b = 1000$. The blue,red and green curves correspond to $a = -100$, $a = -130$ and $a = -160$. From this figure it is clear that this parameter controls the initial part of the distribution. As the value of the parameter a becomes more negative, the initial part of the distribution rises and shows a maxima. As the value of the parameter a becomes less negative, the initial part of the distribution lowers becomes flat. In Figure 45(c), the parameter b has been varied and the other two parameters have been kept constant at $t_h = 0.130$ and $a = -130$. The blue,red and green curves correspond to $b = 500$, $b = 1000$ and $b = 1500$. From this figure it is clear that this parameter controls the final extended part of the distribution. As the value of the parameter b increases, the extended part of the distribution begins to rise. As the value of the parameter b decreases, the final part of the distribution starts to go down and tends to become flat.

3.4.2 Signal fit

Following the procedure as mentioned above, the unbinned data set for the signal was first created using the 'RooDataSet' module of Roofit. Figure 46 shows the unbinned data set for the signal of the mass difference (ΔM) variable. A suitable probability density function needs to be chosen to fit this data set.

Looking at the distribution, fitting was initially tried with a double gaussian (addition of two Gaussian probability denstiy functions), and a Single Crystal Ball probability density function (pdf).

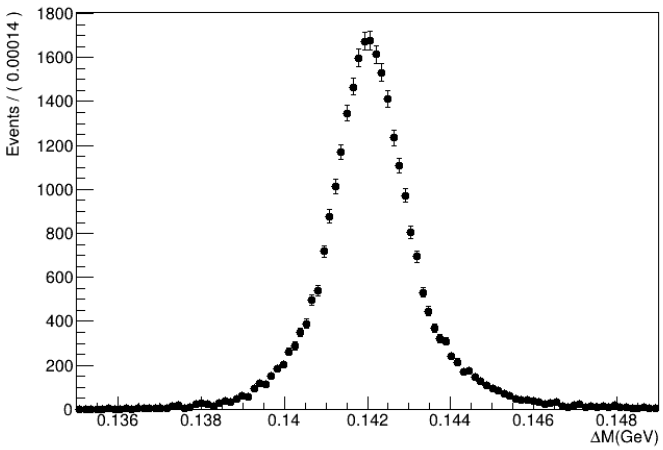

Figure 46: Unbinned data set for the signal

However, from Figure 47, it is clear that these were not good choices of pdfs which could fit the signal data set.

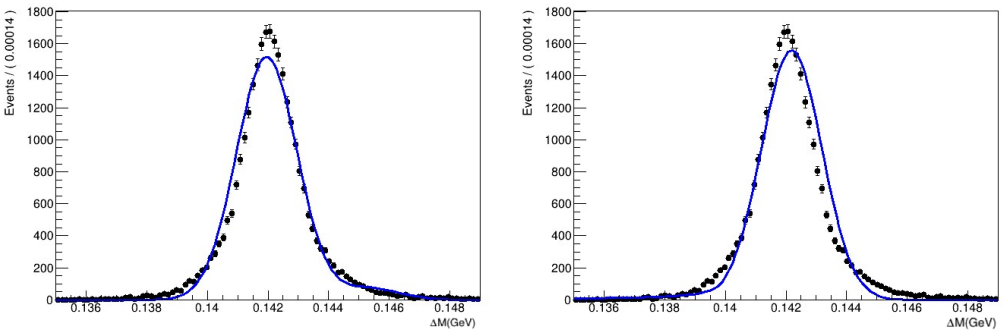

(a) with Double Gaussian pdf

(b) with Single Crystal Ball pdf

Figure 47: Unsuccessful signal fits

Finally with a double Crystal Ball probability density function, a good fit to the signal data set was obtained. Figure 48 shows the outcome of this fit. The solid green and the dashed green curves are the individual Crystal Ball pdfs which when added gave the solid blue curve that fits then data properly. The parameters are all listed in the figure itself. The parameters $n1$, $\alpha 1$ and $\sigma 1$ are of the solid green Crystal ball pdf and $n2$, $\alpha 2$ and $\sigma 2$ are of the dashed green pdf. The joint mean (μ) of these two Crystal Ball pdfs (and hence the solid blue pdf) has a value which is in very good agreement with the expected value of the mass difference ($\approx 0.142 GeV/c^2$)[3]. The χ^2/ndf value is 1.24 which is close to one and the pull distribution is also within ± 3 for the majority of the range of values of ΔM, specially at and near the peak. These indicate that the chosen pdf had properly fit the data set. The obtained probability density function (solid blue curve in figure 48) with its parameters will be incorporated for fitting the signal component in the total data set having both the signal and the background.

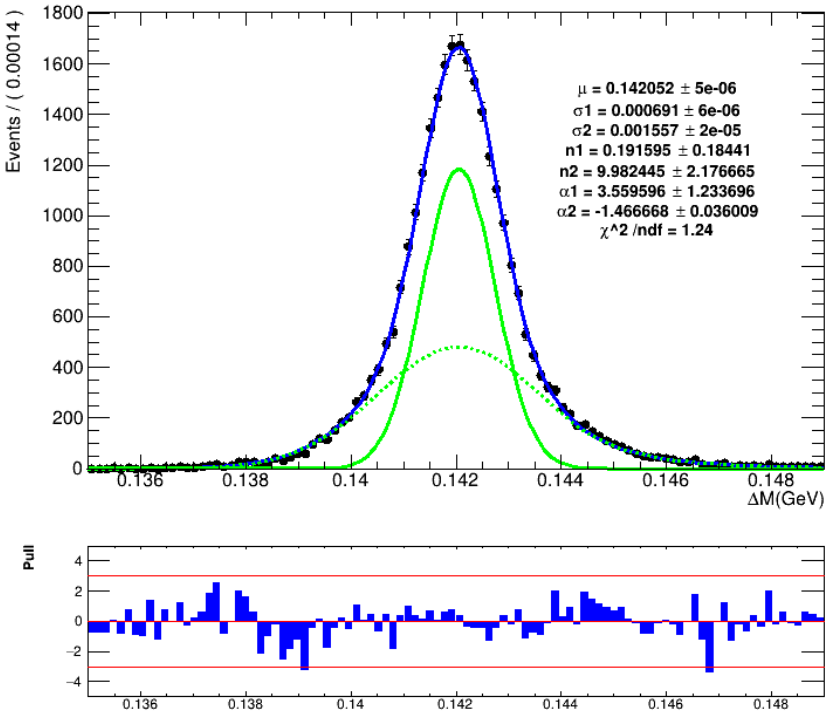

Figure 48: Final fit result of the signal with a Double Crystal Ball pdf. The solid and dashed green curves are the individual single Crystal Ball components of the Double Crystal Ball

3.4.3 Background fit

Following a similar procedure as followed for fitting the signal, the unbinned data set shown in Figure 49 for the background was first created. As seen from Figure 49, this data set contains both the peaking and combinatorial background components. Ideally, one separates the peaking and combinatorial into separate components from the total data set and fits them independently. Thereafter, the two component data sets and the obtained pdfs are added to form the combined fit of the total background. The other way is to fit the total background in a single go by defining suitable pdfs for the peaking and combinatorial parts and adding them, without separating the data set. Both processes involves complexities of their own. The former one involves a complicated fitting procedure where signal and background data sets are separated and then fitted independently. However, this requires less time and there is more control on the fitting parameters as each independent components are fitted independently. In the latter procedure where background data set is not separated into separate components, involves a lot of time as one needs to collectively deal with all the parameters of both the peaking and combinatorial parts together. But the overall fitting procedure is fairly simple as it does not involve dealing the peaking and combinatorial components separately.

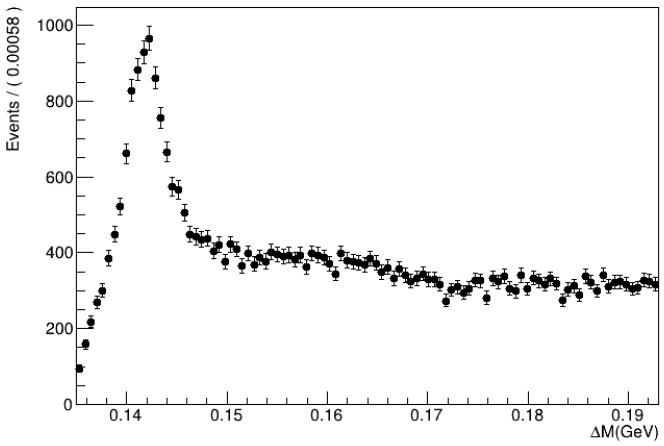

Figure 49: Unbinned data set for the background

The second procedure was used to fit the background. Since for the signal fit, a Double Crystal Ball was found to be effective, for the peaking background, which shows a peak in the signal region, a double crystal ball probability density function was chosen. For the combinatorial part, a threshold pdf as discussed before has been used. These two pdfs were then added and was made to fit the

total background data set in Figure 49. After numerous trials with different set of the parameter values, a proper fit was obtained. The outcome of this fit has been shown in Figure 50.

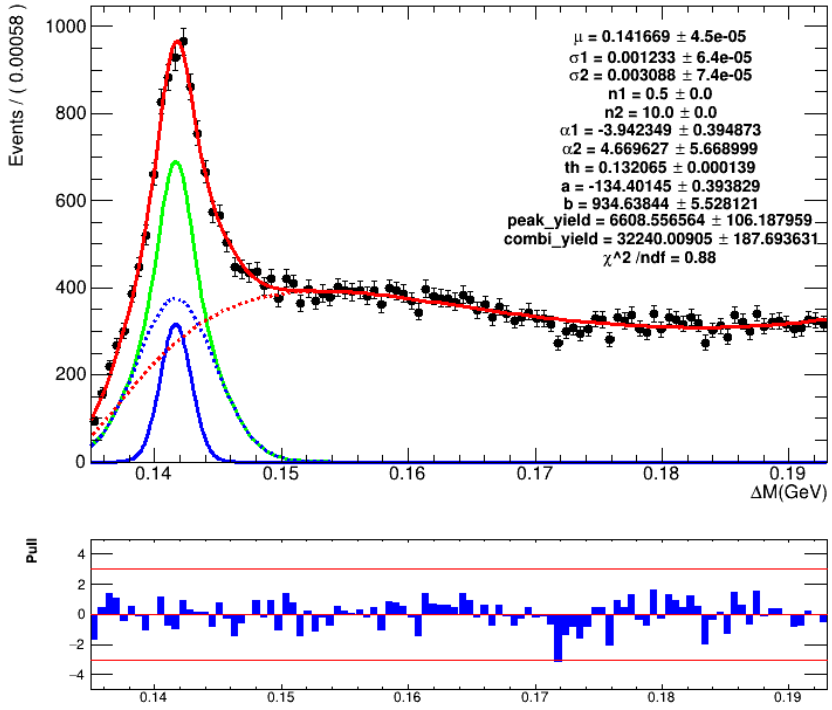

Figure 50: Final fit result of the background (solid red curve) with a double crystal ball for the peaking and a threshold function (dashed red) for the combinatorial components. The solid blue and the dashed blue curves represent the individual Crystal Ball pdfs which when added gives the solid green curve of the Double Crystal Ball representing the peaking background.

The parameter μ represents the mean of Double Crystal Ball pdf used to fit the peaking background. The parameters $n1$, $\alpha 1$ and $\sigma 1$ are of the solid blue Crystal Ball pdf and $n2$, $\alpha 2$ and $\sigma 2$ are of the dashed blue pdf. The parameters $'th'$, $'a'$ and $'b'$ are of the Threshold pdf as discussed before. The combined pdf (solid red curve) provides a good fit to the total background data as indicated by the pull distribution and the value of χ^2/ndf. The pull distribution is within ± 3 throughout the range of values of the mass difference variable and $\chi^2/ndf = 0.88$ which is close to one. From Figure 38(b) it evident that the peaking background and the signal should have a mean close to $0.142 GeV/c^2$. From Figure 48 and Figure 50, the mean's (μ) of the signal and peaking background

are $0.142052 \pm 0.000005 GeV/c^2$ and $0.141669 \pm 0.000045 GeV/c^2$ respectively, both of which are approximately equal to $0.142 GeV/c^2$. Thus from both the signal and background fits, we get the mean value in very good agreement with the expected mean value. The yield's of the peaking and combinatorial backgrounds have also been computed and shown in Figure 50. The peaking background yield comes out to be ≈ 6608 and the combinatorial background yield comes out to be ≈ 32240.

The obtained probability density function (solid red curve in Figure 50) with its parameters will be incorporated for fitting the background component in the total data set having both the signal and the background.

3.4.4 Combined signal and background fit

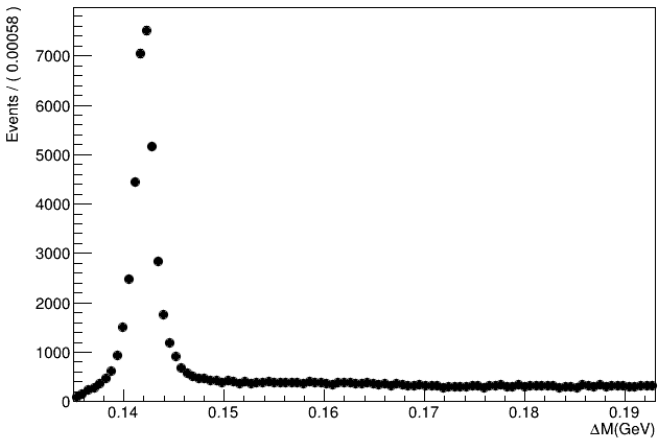

Figure 51: Unbinned data set for the combined signal and background of ΔM

The unbinned data set shown in Figure 51 for the total data set (signal and background combined) was first created. As seen from Figure 51, this data set contains both the signal and background components.

Figure 52 shows the final result of fitting. The probability density functions obtained from fitting the signal and background fitting were added and a total probability density was obtained which fits the total signal and background data set properly. The χ^2/ndf value of this fit is ≈ 0.80 and the pull distribution is within ± 3 throughout the range of values of ΔM. The obtained signal and background mean (μ) have values ($0.142061 GeV/c^2$ and $0.141787 GeV/c^2$ for signal and background respectively) close to the expected value ($\approx 0.142 GeV/c^2$).

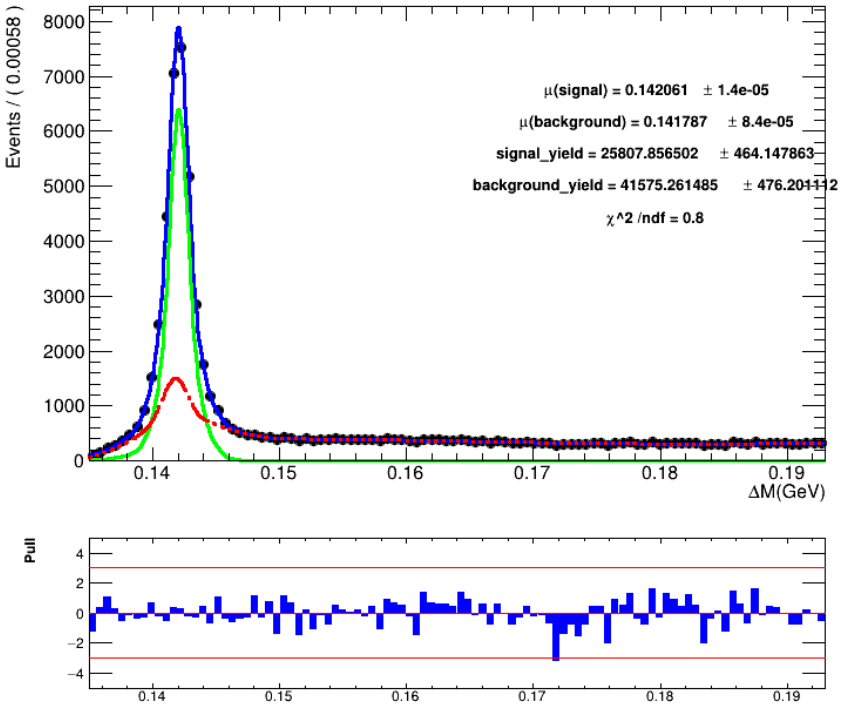

Figure 52: Final fit result of the combined signal and background data set. Green represents the signal pdf, red represents the background pdf and blue represents the total pdf.

The net signal yield and background yield was obtained. The value of the signal yield was obtained as 25808 ± 464 and the value of the background yield was obtained as 41575 ± 476. From Figure 52, the measured mean value of the mass difference of the signal mode, from simulated data comes out as 0.142061 ± 0.000014 GeV/c^2. This is in very good agreement with the currently accepted measured value of the mass difference which is, 0.142014 ± 0.000030 GeV/c^2 as given in PDG[3]. This marks the end of the analysis with simulated data and verifies that our analysis procedure is correct.

4 Results

In this section we discuss the measured value of the relative branching ratio $\Gamma(D^{*0} \rightarrow D^0\pi^0)/\Gamma(D^{*0} \rightarrow D^0\ \gamma)$. The obtained signal selection efficiency after optimization and the obtained signal yield from the combined signal and background fit

for the decay mode $D^{*0} \to D^0\pi^0$ are respectively:

$$\varepsilon_{D^0\pi^0} = 35.02\% \quad and \quad N_{sig}^{D^0\pi^0} = 25808 \pm 464$$

The measured signal selection efficiency and the obtained signal yield with the same $100 fb^{-1}$ of simulated data for the decay mode $D^{*0} \to D^0\gamma$ are respectively[18]:

$$\varepsilon_{D^0\gamma} = 28.32\% \quad and \quad N_{sig}^{D^0\gamma} = 14187 \pm 427$$

The relation between the branching ratios of the above two decay modes with their signal yields and efficiencies are given in equations[19] 4 and 5.

$$\Gamma(D^{*0} \to D^0\pi^0) = \frac{N_{sig}^{D^0\pi^0}}{\varepsilon_{D^0\pi^0} \cdot \mathscr{L} \cdot \sigma \cdot \Gamma(D^0 \to K^-\pi^+)\Gamma(\pi^0 \to \gamma\gamma)} \tag{4}$$

$$\Gamma(D^{*0} \to D^0\gamma) = \frac{N_{sig}^{D^0\gamma}}{\varepsilon_{D^0\gamma} \cdot \mathscr{L} \cdot \sigma \cdot \Gamma(D^0 \to K^-\pi^+)} \tag{5}$$

where $\mathscr{L}$ refers to the integrated luminosity of the experiment (here we are using $100 fb^-1$ of simulated data) and σ refers to the cross section of the production of $c\bar{c}$ pairs in the experiment ($\approx$ 1.3nb in the Belle-II experiment). $\Gamma(D^0 \to K^-\pi^+)$ and $\Gamma(\pi^0 \to \gamma\gamma)$ are absolute branching ratios for the decays $D^0 \to K^-\pi^+$ and $\pi^0 \to \gamma\gamma$ respectively as given in PDG[3].

The relative branching ratio $\Gamma(D^{*0} \to D^0\pi^0)/\Gamma(D^{*0} \to D^0\ \gamma)$ is obtained by dividing the left and right hand sides of equation 4 by equation 5. We get:

$$\frac{\Gamma(D^{*0} \to D^0\pi^0)}{\Gamma(D^{*0} \to D^0\gamma)} = \frac{N_{sig}^{D^0\pi^0}}{\varepsilon_{D^0\pi^0}} \cdot \frac{\varepsilon_{D^0\gamma}}{N_{sig}^{D^0\gamma}} \cdot \frac{1}{\Gamma(\pi^0 \to \gamma\gamma)} \tag{6}$$

On substituting values obtained for the signal yields and efficiencies for both the decay modes in equation 6, we get:

$$\frac{\Gamma(D^{*0} \to D^0\pi^0)}{\Gamma(D^{*0} \to D^0\gamma)} = \frac{25808}{35.02} \cdot \frac{28.32}{14187} \cdot \frac{1}{0.99} = 1.49 \tag{7}$$

We need to calculate the error propagation for the branching ratio. The calculation has been shown equation 6.

$$error = \sqrt{\left(\frac{\Delta N_{sig}^{D^0\pi^0}}{N_{sig}^{D^0\pi^0}}\right)^2 + \left(\frac{\Delta N_{sig}^{D^0\gamma}}{N_{sig}^{D^0\gamma}}\right)^2} = \sqrt{\left(\frac{464}{25808}\right)^2 + \left(\frac{427}{14187}\right)^2} = 0.03 \tag{8}$$

Hence, the measured value of the branching ratio $\Gamma(D^{*0} \to D^0\pi^0)/\Gamma(D^{*0} \to D^0\ \gamma)$ is **1.49±0.03**. This is in good agreement with the world average value of this branching ratio which is 1.85±0.07 as given in PDG[3].

5 Summary and outlook

The decay mode of the charmed meson $D^{*0} \to D^0(K^-\pi^+)\pi^0(\gamma\gamma)$ has been analysed using simulated data (integrated luminosity of $100 fb^{-1}$), which marks the first analysis of this decay mode in the Belle-II experiment. Initially the reconstruction of the decay mode was done in Belle-II software framework using loose pre-selection criteria for the particles. Considerable amount of background was obtained after the reconstruction and hence optimization using the 'cut and count' procedure was done in order to reduce the background so as to isolate the signal. Different variables of the particles present in the decay chain were investigated and discriminating variables showing discrimination between signal and background were selected and optimized. The signal selection efficiency after optimizing all selected variables came as 35.02%. A peaking background was observed after reconstruction which persisted even after optimization. A peaking background study was done to tag the decay modes which contributed to this decay mode. The optimized mass difference distribution of the D^{*0} and D^0 meson (ΔM) was fitted. The mean value of signal from the combined signal and background fit was found to be $0.142061 \pm 0.000014\ GeV/c^2$. A value for the signal yield was obtained (25808 ± 464) which along with the signal selection efficiency, was used to calculate the relative branching ratio $\Gamma(D^{*0} \to D^0\pi^0)/\Gamma(D^{*0} \to D^0\ \gamma)$. The branching ratio was found to be 1.49 ± 0.03. The measured mass difference and relative branching ratio were both found to be in good agreement with their values in PDG.

Any analysis is first done using Monte-Carlo simulated data and then the actual data taken by a detector is allowed to be used. We have completed the work using simulated data. The signal selection efficiency and yield values are crucial inputs for the analysis using actual data. Further work would now be to run on the data taken by the Belle-II detector and measure precise values of the branching ratio and investigate if any new physics is found.

References

[1] Pal, P.B. (2014). An Introductory Course of Particle Physics (1st ed.). CRC Press.

[2] Griffiths, D. Introduction to elementary particles; 2nd rev. version. (Wiley,2008).

[3] Zyla, P. & Others Review of Particle Physics. *PTEP*. **2020**, 083C01 (2020), and 2021 update

[4] Brambilla, N., QCD and strongly coupled gauge theories: challenges and perspectives. *The European Physical Journal C*. **74**, 2981 (2014,10).

[5] Eichten, E., Gottfried, K., Kinoshita, T., Lane, K. & Yan, T. *Phys. Rev. D*. **21**, 203-233 (1980,1).

[6] Cheng, H., Cheung, C., Lin, G., Lin, Y., Yan, T. & Yu, H. *Phys. Rev. D*. **49**, 2490-2507 (1994,3).

[7] Aliev, T., Iltan, E. & Pak, *Physics Letters B*. **334**, 169-174 (1994).

[8] Miller, G. & Singer, *Phys. Rev. D*. **37**, 2564-2569 (1988,5).

[9] Ablikim, M. & Others, Precision measurement of the D^{*0} decay branching fractions. *Phys. Rev. D*. **91**, 031101 (2015).

[10] B. Aubert *et al.* [BaBar], Phys. Rev. D **72**, 091101 (2005)

[11] Abe, T. Belle II Technical Design Report[arXiv:1011.0352 [physics.ins-det]] (2010)

[12] Matvienko, D. The Belle II experiment: status and physics program. *EPJ Web Of Conferences*. **191** pp. 02010 (2018,1)

[13] Belle II Software Documentation, https://software.belle2.org

[14] Belle-II confluence page: https://confluence.desy.de/display/BI/Software+Basf2Introduction

[15] Sharma C., Lalwani K. & Di Canto A., Rediscovery of "wrong-sign" D^0 decays to hadronic final states with early Belle II data, BELLE2-NOTE-PH-2020-032.

[16] Casarosa G. & Di Canto A., Measurement of the D^0 lifetime, BELLE2-NOTE-PH-2020-033.

[17] Patra S. & Bhardwaj V., MC decay tagging using generated level information with GenMCTagTool, BELLE2-NOTE-TE-2021-002.

[18] Das A., Analysis of the decay mode $D^{*0} \to D^0(K^-\pi^+)\gamma$ in Belle-II experiment. *M.Sc project thesis*, Indian Institute of Technology Bhubaneswar.

[19] Kou, E. & Others, The Belle II Physics Book. *Progress Of Theoretical And Experimental Physics*. **2019** (2019,12).